energies

Article

Comparing the Utility of Coupled Aero-Hydrodynamic Analysis Using a CFD Solver versus a Potential Flow Solver for Floating Offshore Wind Turbines

Mohd Atif Siddiqui [1], Finn-Christian Wickmann Hanssen [1,2,*], Marilena Greco [2,3] and Eirik Anda [2]

[1] Semar AS, Strandveien 12, 1366 Lysaker, Norway; atifsiddiqui2008@gmail.com
[2] Department of Marine Technology, Norwegian University of Science and Technology (NTNU), 7049 Trondheim, Norway; marilena.greco@ntnu.no (M.G.)
[3] Institute of Marine Engineering (CNR-INM), Via di Vallerano 139, 00128 Rome, Italy
* Correspondence: finn-christian.hanssen@ntnu.no

Abstract: There has been a great effort towards development of renewable energy systems to combat global warming with significant interest towards research and development of floating offshore wind turbines (FOWTs). With commercial projects such as Hywind Scotland, Hywind Tampen and others, there is a shift of industry attention from bottom-fixed offshore turbines to FOWTs. In this work, we focus on comparing industry standard Potential Flow (PF) methods versus Computational Fluid Dynamics (CFD) solvers for a scaled version of the IEA 15 MW turbine and associated FOWT system. The results from the two solvers are compared/validated using experimental thrust values for the fixed turbine. The motions and the thrust for the FOWT system are then compared for the two solvers along with hydrodynamic properties of the floater hull. The wake features downstream of the turbine are analyzed for the fixed and floating turbine using the CFD solver. The wake from the CFD solver is also compared with a simplified PF model. Finally, a simplified cost-benefit analysis is presented for the two solvers to compare the usefulness and utility of a CFD solver as compared to presently used industry-standard PF methods.

Keywords: floating offshore wind turbine; CFD; potential-flow methods; renewable energy

check for updates

Citation: Siddiqui, M.A.; Hanssen, F.-C.W.; Greco, M.; Anda, E. Comparing the Utility of Coupled Aero-Hydrodynamic Analysis Using a CFD Solver versus a Potential Flow Solver for Floating Offshore Wind Turbines. *Energies* **2023**, *16*, 7833. https://doi.org/10.3390/en16237833

Academic Editor: Davide Astolfi

Received: 6 November 2023
Revised: 21 November 2023
Accepted: 24 November 2023
Published: 28 November 2023

Copyright: © 2022 by the authors. Licensee MDPI, Basel, Switzerland. This article is an open access article distributed under the terms and conditions of the Creative Commons Attribution (CC BY) license (https://creativecommons.org/licenses/by/4.0/).

1. Introduction

Floating offshore wind turbines (FOWTs) have been studied extensively from the 2000s due to the increasing need to shift to renewable sources of energy and the significant potential for development of offshore wind in deep-water sites with large prevailing wind velocities. Along with this, there has also been a shift from academic interest to industrial and commercial projects. FOWTs are complex systems with extensive interaction between aerodynamic loads on the rotor nacelle assembly (RNA), structural deformation of the rotor blades and supporting tower, hydrodynamic loads on the floater hull coupled with a mooring system and power cables, and the control modeling of the turbine (see Figure 1). To design and dimension these systems, it is thus important to model critical physical aspects as accurately as possible. Turbine capacities are quickly increasing from 5 to 8 MW (Hywind Scotland and Hywind Tampen) towards designs with 15 MW (already being tested) and even 20 MW. Such large structures, with rotor diameters in the order of 200 m or larger, pose challenges for the numerical modelling. Matha and Schlipf [1] discussed exhaustively such challenges along with the pros and cons of potential flow (PF) vs. Computational Fluid Dynamics (CFD) methods. Otter et al. [2] provided a comprehensive review of experimental and numerical modelling of FOWTs, where tools were classified as “low”, “mid”, and “high” fidelity. As in all numerical modelling involving approximations, there is an inherent trade-off between accuracy and efficiency. PF methods (classified as “mid-fidelity” methods by Otter et al. [2]), which assume in-viscid and irrotational flow and an incompressible fluid, are generally used to calculate hydrodynamic loads on structures, combined with simplified models for possible rotational and viscous flow effects. These provide efficient numerical solutions that represent loads and motions with good accuracy for large-volume structures, and are therefore widely used in marine/ocean engineering. CFD methods, on the other hand, inherently account for viscous and other nonlinear effects and are classified as "high-fidelity" methods by Otter et al. [2]. However, they are much less efficient than PF methods, thus requiring significant computational resources.

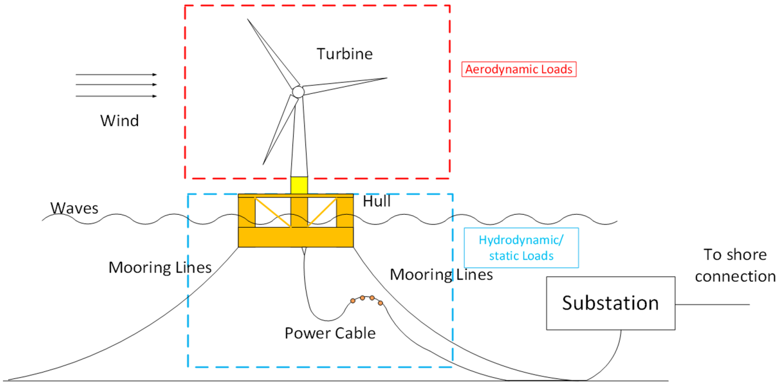

Figure 1. Basic components of a floating wind turbine along with the key physical effects.

There are several codes, both commercial and open-source, that have been used to numerically model FOWT systems. FAST [3] is a widely used open-source software developed by the National Renewable Energy Laboratory (NREL) that is composed of several individual modules, which are coupled in a time domain aero-hydro-elastic-servo solver. Recently, FAST was renamed to OpenFAST. Orcaflex [4] is a commercial software for general modelling of floating dynamic systems, which during recent years has been given the possibility to perform aero-hydro-elastic-servo simulations for FOWTs, including extensive validation against OpenFAST results. Both OpenFAST and Orcaflex use hydrodynamic coefficients from well-documented frequency-domain Boundary Element Method (BEM) solvers such as Wamit as input to represent wave loads. Structural loading/deformations of the turbine tower and rotor blades are described using the Finite Element Method (FEM) combined with the Blade Element Momentum Theory (BEMT) to resolve aerodynamic loads. The FEM is also used to describe the behaviour of mooring lines. The respective solvers for the various system components are coupled in time domain. Several studies examining the capabilities of the two codes are available in the literature, and a few relevant works are described in the following.

Dagher et al. [5] presented an extensive study for three floating platforms supporting the NREL 5 MW turbine at a 1:50 scale and compared experiments with FAST simulations, showing good agreement for wind-only cases but with some discrepancies when waves were included. Stewart et al. [6] presented a comparison of a calibrated FAST model against experimental data for a tension leg platform (TLP) FOWT, with good agreement in the wave-excitation frequency range. Wang et al. [7] found good agreement between numerical (OpenFAST) and experimental results during investigation for a 5 MW OC3 spar-type FOWT at a scale of 1:50. The reasons for the differences in the results of the FOWT under wind, wave, and current conditions were discussed. Kim and Shin [8] performed validation of a numerical FAST model against experiments for a 1:40 scale 750 kW FOWT for various load cases. They found good agreement between the numerical model and experiments for surge and heave motions, but larger differences for pitch motion. Ahn and Shin [9] compared results from FAST and an in-house code with experimental results for a 10 MW FOWT model at scale 1:90 with good agreement. Thomsen et al. [10] studied the "TetraSpar" floater concept and investigated the use of new modelling approaches in Orcaflex and OpenFAST for the numerical representation of the floater hull. For this specific concept, modelling the hull as either rigid or flexible gave considerable differences. Vittori et al. [11]

performed experiments for a 1:49 scale model of a 10 MW FOWT system and compared with OpenFAST numerical results. They noted that the pitch natural frequency shifts with wind loading on the FOWT system. This effect could not be captured in the simulations, since the numerical model does not update the hydrostatic restoring when the hull is tilted. In addition to the ones referenced here, there are several other studies with similar experimental and numerical analysis showing reasonable or good agreement. Among the reasons for observed differences between experimental and numerical results, the inherent limitation of potential flow theory has been suggested. PF solvers generally represent hydrodynamic (and hydrostatic) loads based on a linear solution, and viscous loads are at best represented in an approximate manner. Several researchers have tried to improve the simulation accuracy by using CFD solvers in different ways. However, CFD simulations for FOWTs present their own set of challenges ranging from complex setup to high-resource computational requirements. In addition, the CFD setup and associated assumptions (including turbulence modelling, neglecting structural blade deformation, etc.) imply that these simulations should not by default be perceived as superior to PF solvers. However, with proper setup and experience-based modelling choices in both aerodynamic and hydrodynamic modelling, accurate "high-fidelity" CFD simulations can be achieved. In addition, CFD captures flow phenomena such as turbine wakes in a way that PF methods cannot.

Traditionally, CFD methods have been used in the floating wind industry to better understand the hydrodynamics of floater hulls for FOWTs or to simulate the aerodynamics for the rotor. For CFD modelling of (fixed) land-based wind turbines, a variety of literature exists and a few important references are mentioned in the following with particular focus on the use of the open-source code OpenFOAM (OF). Sanderse et al. [12] reviewed state-of-the-art CFD simulations of wind-turbine wake aerodynamics, and discussed techniques for modelling the rotor and the wake including turbulence models. Tossas and leonardi [13] discussed the implementation of the actuator line model (ALM) and actuator disk model (ADM) using OF. Stergiannis et al. [14] studied the differences in modelling a rotor wake using CFD through the ADM model and a full rotor model. They found that the wake behind the turbine using the two approaches can be quite different and, therefore, the choice of model representing the best compromise between accuracy and efficiency should be made based on the parameters of interest. For example, for estimation of loads on the rotor, ADM is more efficient without sacrificing accuracy, whereas to analyse wake features a full rotor model is needed.

Numerous authors have studied the hydrodynamic loads of floater hulls using CFD excluding the turbine and associated aerodynamics, but considering the structural mass/inertia of the tower, turbine blades and RNA. Among them, Beyer et al. [15] analysed surge free-decay tests using the Navier–Stokes (NS) equations for the OC3 spar model in turbulent flow conditions. Benitz et al. [16,17] performed turbulent-flow CFD simulations to calculate hydrodynamic loads on the OC4 semi-submersible floater hull in current and waves, highlighting the presence of shadow effects behind the columns of the semi-submersible hull. Rivera-Arreba et al. [18] performed laminar-flow CFD simulations for heave and pitch free-decay of the OC5 semi-submersible. In addition they performed simulations in regular waves, and found differences between CFD and PF results for large-steepness wave cases. Nematbakhsh [19,20] performed laminar-flow CFD simulations for a tension-leg platform (TLP), where they conducted free-decay tests in surge and heave, and computed the regular-wave response using the level-set (LS) method to model the free-surface deformations. Li and Bachynski [21] compared nonlinear diffraction wave loads on the OC6 floater with CFD and a PF hybrid model (the latter including Morison elements to approximate viscous loads), discussing the advantages of using CFD for estimation of higher-order loads. They also discussed the effect of a mean pitch angle (tilted hull geometry) on diffraction loads. Li and Bachynski [22] proposed a method for correcting quadratic transfer function (QTFs) for wave-drift loads obtained from PF using CFD data, and demonstrated that the modified QTFs improved the agreement with experimental data. In addition, Galera-Calero et al. [23] performed numerical simulations for a semi-submersible FOWT platform using the commercial CFD code Star-CCM+, showing reasonable agreement between numerical results and experimental results obtained in the LIR/NOTF wave basin by Saitec Offshore Technologies.

Recently, with a general increase in CFD capability and availability of computational power, CFD studies on coupled aero-hydrodynamics of FOWTs have been performed. In this framework, Xu et al. [24] provided an exhaustive review on CFD simulations for FOWTs. The authors discussed the advantages of using CFD for fully coupled simulations, including detailed resolution of wake flow-field features. Among the drawbacks and shortcomings mentioned are high computational requirements, the lack of studies capturing blade deformation for large turbines (aero-hydro-elastic studies), and the lack of studies with realistic modelling of turbine inflow conditions. Liu [25] and Liu et al. [26] performed fully coupled aero-hydrodynamic simulations of FOWTs using OF, comparing results against industrial/engineering codes (e.g., OpenFAST) with reasonable agreement. In addition, these works discussed the advantages of using CFD, including high-detail representation of the wake field behind the turbine. Such representation of the wake field makes it possible to analyse the inflow for downstream turbines more realistically, and can thus serve as a tool to optimize the layout/area of floating wind farms. Zhou et al. [27] expanded on the work of previous authors comparing CFD simulations with OpenFAST results, stating that nonlinearity of wave loads in steep waves causes differences between CFD and other methods. Cheng et al. [28], Huang and Wan [29], analysed the fully coupled aero-hydrodynamic model for a FOWT with an in-house OpenFOAM-based solver called naoe-FOAM-SJTU for the hydrodynamics combined with an Unsteady Actuator Line Model (UALM) for the aerodynamics. The authors concluded that the UALM model resolves the flow with reasonable accuracy when compared to BEMT models, but less accurate (albeit more efficient) when compared to full rotor modelling. Tran and Kim [30] performed coupled aero-hydrodynamic simulations for a floating turbine focusing on the surge motion, concluding that the power production of the turbine is influenced by the platform surge motion. Tran and Kim [31] performed aero-hydrodynamic coupled CFD simulations also including mooring line dynamics for the DeepCwind floating platform and the NREL 5-MW turbine. A prescribed motion was enforced to the platforms, and comparisons with experiments and FAST showed good agreement. Tran and Kim [32] extended their previous work incorporating fluid–structure interaction for the rotor blades allowing platform motions in six degrees of freedom (DOF), and showed good agreement with FAST. Liu et al. [33] extended their CFD work for the NREL 5 MW turbine, coupling the CFD solver with a code to solve the structural deformations of the rotor blades and forcing the turbine to move sinusoidally in surge. Differences between the CFD solver and FAST were observed, and between CFD simulations with rigid and deforming blades, respectively. Arabgolarcheh et al. [34] performed CFD simulations for a 5 MW FOWT using the ALM method, concluding that, as expected, the ALM modelling provides efficiency compared to full rotor models. Zhang and Kim [35] also compared BEMT and CFD codes, and showed that for a fixed turbine, the results for the two approaches were relatively similar. However, for a floating system, there were differences in the thrust from the two solvers. The wake behind the FOWT system was also discussed in detail.

Although a few are mentioned above, a relatively limited number of studies have been published where the aero-hydrodynamic coupling for FOWTs using CFD and PF solvers is compared. Even fewer studies have considered the aero-hydrodynamic-structural coupling for FOWTs. The aim of the present research is to extend the work of aforementioned researchers to a larger turbine and associated floater hull, since most of the published studies use a 5 MW turbine in their analyses. With the global trend in the floating wind industry to deploy larger turbines of 10 MW and beyond, larger aerodynamic and hydrodynamic nonlinear loading effects appear. As a starting point, the open-source IEA 15 MW turbine (defined in Gaertner et al. [36]) along with the associated open-source Volturn US-S floater hull (defined in Alle et al. [37]) is selected. Due to computational limitations and to validate the solvers used, the scaled version of the IEA 15 MW turbine defined in Kimball et al. [38]

and Mendoza et al. [39] is studied, for which Mendoza et al. [39] has provided experimental results for a "performance-matched" model turbine in varying wind, rotor speed and blade pitch conditions. The main aim of the performed work is to further explore the utility of PF (using Orcaflex) versus CFD (using OpenFOAM) methods for solving FOWT systems, as a contribution to continue building knowledge for the floating wind community. To assess the solver accuracy, we compare fixed-turbine thrust results obtained with the PF and CFD solvers against the aforementioned experiments from Mendoza et al. [39] for a load case. Hydrodynamic aspects related to the floater hull (excluding the RNA and tower) are examined using both PF and CFD. Challenges related to accurate modelling of large turbines and subsequently larger floating substructures in CFD are highlighted.

The present study is an extension of the work presented in Siddiqui et al. [40]. A fully aero-hydrodynamic coupled FOWT model (including floater hull and turbine) is implemented in OF, where the floater is allowed to move freely in pitch while disregarding rotor blade deformations. The same setup is modelled in the PF solver to allow for a proper comparison of the turbine thrust between the two solvers. The differences in the wake-flow features between the fixed and floating turbines are studied using the CFD solver. Furthermore, the wake field obtained with the CFD solver is compared with a simplified model described in de Vaal and Muskulus [41]. Finally, a qualitative cost-benefit analysis is presented comparing the usefulness and utility of CFD methods relative to industry-standard PF methods for the analysis of FOWTs. The paper is structured as follows: Section 2 provides a brief description of the properties of the IEA turbine and Volturn US-S floater including the properties for the scaled turbine and the scaling method. The simulation scenarios with related parameters are provided in Section 3. The theoretical background for the PF and CFD solvers is described in Section 4, including the associated boundary conditions, numerical setup, mesh generation, and simulation parameters. Methods for data analysis to obtain hydrodynamic and aerodynamic quantities of interest are described in Section 5. Results and discussion are provided in Section 6, before the conclusions and suggestions for future work are given in Section 7.

2. Floating System Specification

Commercial FOWT designs with their specific turbines and associated floating substructures are generally copyrighted designs, lacking publicly available data required for numerical modelling. In this regard, open-source reference turbines are important tools for researchers and industry, being publicly available and extensively benchmarked and facilitating collaborative efforts. The International Energy Agency (IEA) 15 MW turbine, having a size significantly larger than the NREL 5 MW turbine, which has been extensively studied in referenced literature, is currently the largest available reference turbine openly available Gaerter et al. [36]. With the size of turbines in offshore wind sector rapidly increasing ([42]) to harvest higher prevailing wind resources with fewer units, the IEA 15 MW turbine is therefore used in the present work with the following rationales:

- Aligning the research output with the current and future industry trends;
- Providing insight into aspects potentially associated with larger-size turbines such as:
    1. Increased floater hull motions and larger nonlinear viscous loads;
    2. Challenges in numerical modelling.

In addition, an ambition is to provide a reference for future research involving large turbine sizes.

As floating substructure, the UMaine Volturn US-S semi-submersible specifically designed by the University of Maine to support the IEA 15 MW turbine (Allen et al. [37]) is adopted. Allen et al. [37] also specifies system components such as mooring, controller, etc. The floater is an open generic steel version of the patented UMaine concrete design (see Figure 2). Dimensions and properties of the turbine and floater are shown in Tables 1 and 2, respectively.

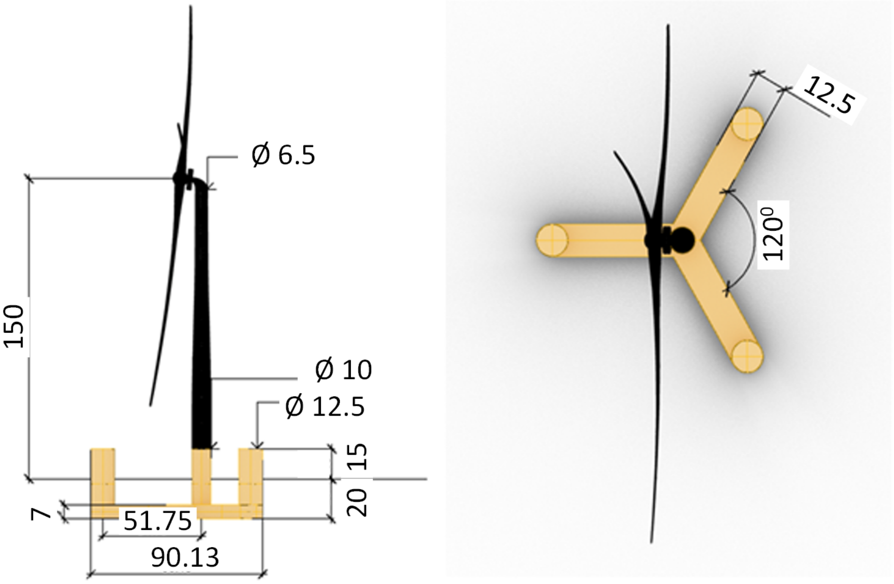

Figure 2. The IEA 15 MW turbine with the supporting UMaine Volturn US-S semi-submersible floater hull with main dimensions (lengths are in meters).

Table 1. Main particulars of the IEA 15 MW reference turbine.

Property	Value
Rated power (MW)	15.0
Class	IEC Class 1B
No. of blades	3
Rotor diameter (m)	240
Hub height (m)	150
Cut-in/rated/cut-out wind speed (m/s)	3.0/10.6/25.0
RNA mass (t)	991
Maximum tip speed (m/s)	95

Table 2. Main particulars of the UMaine Volturn US-S Floater.

Property	Value
Outer columns diameter (m)	12.5
Central column diameter (m)	10
Column height (m)	35.0
Pontoon width (m)	12.5
Pontoon height (m)	7
Centre-centre distance (m)	51.75
Total substructure mass (t)	17,839
Displacement (t)	20,093
Draft (m)	20
Roll radius of gyration R_{xx} (m)	24.91 [1]/47.12 [2]
Pitch radius of gyration R_{yy} (m)	24.91 [1]/47.12 [2]
Yaw radius of gyration R_{zz} (m)	34.301 [1]/34.52 [2]

[1] For floating substructure only; [2] For entire FOWT system.

Scaled IEA 15 MW Model Wind Turbine

Originally, the aim was to compare results from a PF solver with CFD simulations for the full-scale IEA 15 MW turbine. During initial simulations, however, it was realized that a proper representation of the geometry and refinement of the associated flow field at full scale was required in the order of 50 million cells in CFD. With the available computational resources, this made full-scale simulations infeasible. This was especially the case for longer wave periods, requiring a large computational domain together with significant simulation time. To mitigate this, it was decided to instead use a reduced-scale turbine for comparison with PF results. In addition, moving from full scale to model scale justifies the use of laminar flow conditions due to reduced values of Reynolds number, (Re). It is to be noted that the model-scale FOWT is only used for cases where the (fixed or floating) turbine aerodynamics are simulated. For cases without the turbine, i.e., pure hydrodynamic analysis, the required number of cells is substantially reduced and the studies are performed with the full-scale floater.

For the scaled turbine, the scaling method and scaled turbine design are briefly discussed in the following with details provided in Mendoza et al. [39]. The Floating Offshore Wind and Controls Advanced Laboratory (FOCAL) Experimental Program aims at performing model scale tests and providing results for validation of fundamental concepts necessary for FOWT controls design. In relation to the FOCAL project, Kimball et al. [38] presented a scaled-down design (1:70 scale) for the IEA 15 MW turbine. Froude scaling was assumed, i.e., the Froude number is kept equal in full and model scale. The Froude number is given as $Fr = U/\sqrt{gL}$ where U is the characteristic velocity, g is acceleration of gravity, and L is the characteristic length scale. Table 3 provides the relevant scaling factors for various physical quantities with length scale parameter Λ (i.e., the ratio between model-scale and full-scale length).

Table 3. Scale factors for various physical quantities following the Froude scaling law.

Quantity	Scale Factor	Scale Factor 1:70
Length (wave height, lengths)	Λ	70
Time (wave period)	$\Lambda^{0.5}$	8.37
Velocity (wind speed)	$\Lambda^{0.5}$	8.37
Angle	Λ^{0}	1
Angular velocity	$\Lambda^{-0.5}$	0.119
Frequency (rpm)	$\Lambda^{-0.5}$	0.119
Mass	Λ^{3}	343,000
Mass moment of inertia	Λ^{5}	1.68×10^{9}
Volume	Λ^{3}	343,000
Force (thrust)	Λ^{3}	343,000
Torque	Λ^{4}	2.401×10^{7}
Power	$\Lambda^{3.5}$	2.87×10^{6}

Froude scaling is widely used in hydrodynamic model testing of large-volume fixed and floating marine structures to proper model the response due to gravity waves. However, with atmospheric pressure and Froude scaling it is not possible to have similarity of viscous loads (i.e., the Reynolds number will be smaller at model scales). As seen in Table 3, scaling down the full-scale turbine power of 15 MW with a scale factor of $\Lambda = 1/70$ gives a model-scale power of $P_M = P_F/\Lambda^{3.5} = 15/70^{3.5} = 5.23$ W, while the rated wind speed becomes $U_M = U_f/\Lambda^{0.5} = 1.27$ m/s. This causes an inconsistency as the performance of the airfoil sections used for the IEA 15 MW turbine blades varies significantly at lower Reynolds numbers. The Reynolds number associated with a generic blade cross-section, i.e., with an airfoil, can be defined as $Re = Uc/\nu$, where U is the characteristic velocity, c is the characteristic length, coinciding with the chord length for an airfoil, and ν is the kinematic viscosity of the fluid (air in this case). Operating at smaller Re (such as in model scale), the airfoils will produce less lift and more drag, thus giving less power than the corresponding Froude-scaled value of 5.23 W. To mitigate this inconsistency, a new blade design with a different airfoil geometry and associated blade properties was proposed. The new turbine design with lower Re airfoils is labelled a "performance matched" design, preserving the thrust (and power) at Froude-scaled rated wind speeds and rated revolutions per minute (RPM). The airfoil applied in this model (SD7032) has lower thickness-to-chord ratio than the original design and experiences lower drag and higher lift at model scale than the original Froude-scaled design. The geometric properties of the new blade design are defined in detail in Kimball et al. [38], and were used to construct a 3D CAD model (as shown in Figure 3). The main particulars of the model-scale FOWT are listed in Table 4.

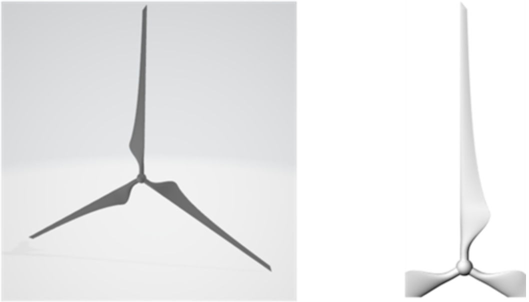

Figure 3. CAD model of the performance matched model-scale blade design perspective (**left**) and front view (**right**).

Table 4. Physical properties of the model-scale FOWT system.

Properties	Model Scale Value
Hub height (m)	2.140
Rotor diameter RD_M (m)	3.468
Shaft tilt (deg)	6.000
Wind speeds U_{WM} (m/s)	0.400–3.600
Rated RPM in rad/s	6.130
Rated thrust (N)	6.660
Blade mass (kg)	0.236
Blade second mass moment of inertia (kgm^2)	0.116
Total Rotor Mass (kg)	0.708
Floater hull displacement (kg)	58.4

3. Simulation Cases and Parameters

The CFD simulations are divided in two parts:

- Hydrodynamic floater hull only cases, in full scale defined in Table 5;
- Coupled aero-hydrodynamic floater-and-rotor cases, in model scale 1:70 defined in Table 6.

Table 5. Simulation cases and parameters for floater hydrodynamics.

Case	Analysis Type	Parameters	Qty. of Interest
1	Diffraction	Wave periods T = 6, 8, 10, 12 s Wave heights H = 3 m, 6 m 0° and 180° heading Mean pitch angle of 5°	1st order loads
2	Radiation (forced motion)	Forcing periods T_f = 6, 10, 15 s Heave ampl. A_f = 0.5, 2 m Pitch ampl. θ_f = 2.5°, 5°	Added mass Damping
3	Free decay	Heave and pitch motion	Resonance period Damping
4	Fixed floater in uniform current	0° and 180° heading Current velocity U = 1 m/s	Drag loads

Table 6. Simulation cases and parameters for coupled aero-hydrodynamics of the floater and rotor.

Case	Analysis Type	Parameters	Qty. of Interest
5	Fixed turbine in uniform wind	Wind velocity U_{WM} = 1.2 m/s Rotor angular velocity 6.13 rad/s Pitch of rotor blades	Thrust
6	Hull (free to pitch) and rotor in wind and waves	Wind velocity U_{WM} = 1.2 m/s Rotor angular velocity 6.13 rad/s H = 0.071 m, T = 0.71 s 0° heading	Thrust Mean pitch motion

The air and water densities are 1.25 kg/m^3 and 1025 kg/m^3, respectively, and the full-scale water depth is taken as 150 m (corresponding to 2.143 m in model scale). The seabed is assumed to be flat. The kinematic viscosities of water and air are taken as 10^{-6} m^2/s and 1.48×10^{-5} m^2/s, respectively. Other relevant quantities are described in individual case setups.

4. Analysis Tools

PF time-domain simulations of the coupled RNA and floater system are performed in Orcaflex with hydrodynamic coefficients used as input computed in the radiation-diffraction code WADAM ([43]). The open-source code OpenFOAM, with its built-in packages for pre-processing, numerical solution and post processing, is used to perform CFD simulations.

4.1. Potential Flow Solver

First-order added mass and damping coefficients and transfer functions for first-order wave excitation loads and second-order mean wave drift loads for the floater hull are taken from frequency domain analysis in WADAM with the mean wetted part of the hull discretised using quadrilateral planar panels (see Figure 4). The appropriate panel size (δl) is established through a convergence study considering three meshes, i.e., "coarse", "medium", and "fine". Properties for the meshes are given in Table 7. The convergence study is performed for the mean wave drift loads, which are typically the results from such analysis that are slowest to converge. The mean wave drift loads are calculated using the Conservation of Fluid Momentum (CFM) method, since it is known that results obtained with the alternative method of Direct Pressure Integration (DPI), within a perturbation approach using inertial reference frame, are more sensitive to the size and shape of panels near the free surface. In fact, Shao [44] showed that a main reason for differences between DPI and CFM can be the presence of sharp corners in the body, and hence DPI in some cases may never fully converge regardless of the panel size.

Based on the analysis, the "medium" mesh is found to give converged results, and results for this mesh are therefore imported into the Orcaflex model. The frequency domain analysis covers wave periods 3–40 s with an increment of 0.5 s for headings 0–180° with an increment of 30°. The analysis to establish hydrodynamic coefficients was performed using an external quadratic damping matrix with values defined in Allen et al. [37] to approximate viscous damping effects.

Table 7. Details of mesh sizes for PF solver.

Mesh Name	Average Panel Edge Length (m)	Total Number of Panels
Coarse	1.25	5034
Medium	1.00	9472
Fine	0.80	12,618

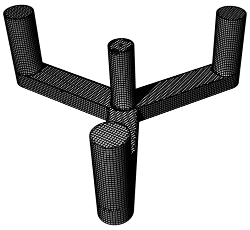

Figure 4. Medium panel models of the floater hull used in convergence study.

Orcaflex is a software package for dynamic analysis of marine systems including functionality to build up wind turbine systems, where turbine blade data can be inserted in terms of geometric and aerodynamic data. The wind loads on the turbine are modelled using a blade element momentum (BEMO) theory model. For wind generation, a constant wind profile is used. The wind loads on the turbine are coupled with the hydrodynamic loads on the floater in time domain while the wind loads on the turbine tower and the floating foundation are neglected, along with structural deformation of the turbine blades (although Orcaflex offers such capabilities). This is to provide a direct comparison with the CFD model where these aspects are neglected. The blade properties (wing type, aerodynamic properties, inertia properties, etc.) are taken from Kimball et al. [38] and used to setup the "turbine" object in Orcaflex (see Figure 5).

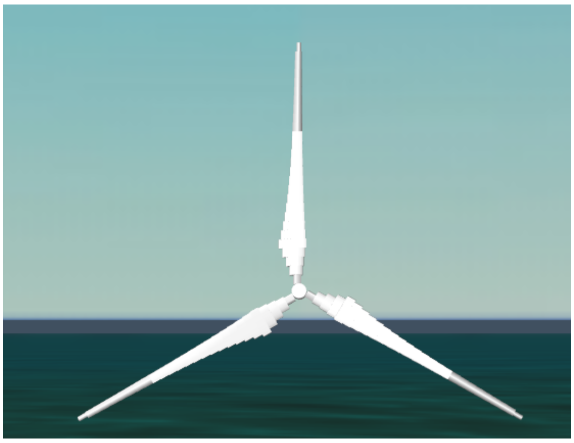

Figure 5. Scaled IEA turbine model setup in Oracflex.

4.2. CFD Solver

OpenFOAM (OF) is an open-source environment based on the Finite Volume Method (FVM) and implemented using C++ templates developed initially by H. Weller and H. Jasak [45] that can be employed to simulate a variety of fluid–body interaction problems. OF runs well on parallel processors, and being a freely available open-source code, can be modified to add new functionalities. The user manual ([46]) provides in-depth details on implementation of the governing equations, solution algorithms, solver settings, and boundary conditions, with a few main aspects discussed briefly in the following. Any deviation from the general description provided below will be defined in the relevant sections.

4.2.1. Solver Settings

The viscous flow is governed by the nonlinear Navier–Stokes (NS) equations, which are solved simultaneously with the continuity equation in the fluid domain (air and/or water) resulting in a coupled pressure-velocity equation system. Here, these are solved using the PIMPLE method, which is a combination of PISO (Pressure Implicit with Splitting of Operator) and SIMPLE (Semi-Implicit Method for Pressure-Linked Equations). The number of inner iterations (pressure correction for SIMPLE) and outer iterations (pressure correction for PISO) are set to 2, which ensures convergence within the present studies.

With the presence of both air and water the NS equations must be solved for both of these phases, resulting in a two phase system. The Piecewise-Linear Interface Calculation (PLIC) scheme, which is an improved version of the Volume-of-Fluid (VoF) technique proposed by Hirt and Nicholas [47], is used by OF to estimate the air–water interface where an additional transport equation for the volume fraction (α) emerges. This is evolved in time in OF with the MULES (Multidimensional Universal Limiter with Explicit Solution) solver. The time-stepping method in the solution algorithm is adaptive with variable time steps depending on the average flow features to ensure stability following from a maximum Courant number (Co) criterion. Here, the maximum Co is set to 1 and the maximum interface Courant number (Co_{pf}) is set to 0.5. A first-order implicit Euler scheme is used for time-evolution of the equations. The position of the free surface is estimated by locating the contour where $\alpha = 0.5$. Spatial terms are discretized with a second-order scheme. The main machine used to perform the simulations is an AMD Threadripper processor with 32 physical cores (4 GB RAM per core). In addition, some nodes from UNINETT Sigma2—the National Infrastructure for High Performance Computing and Data Storage in Norway were made available.

4.2.2. Domain Size and Boundary Conditions

Separate domain and boundary condition setups are used for the floater hull only cases in Table 5 and the floater plus rotor cases in Table 6.

Floater hull only: A two-phase 3D Numerical Wave Tank (NWT) is established in OF with a 2D cut parallel with the xz plane shown in Figure 6. The left plot of the figure shows the setup for the diffraction, forced motion and free decay simulations whereas the right plot shows the setup for the simulations with a fixed floater in uniform current. The height of the NWT is 190 m with a water depth d of 150 m, whereas the length L is modified for the diffraction case with largest wave period and for the larger forcing/free decay period. The free surface lies entirely within the zone $|z| < 0.5d2$ and the floater lies entirely in zone $|z| < 0.5d1$. To resolve the free surface and flow features close to the structure with sufficient accuracy, the cells in the z-direction are divided in half two times; first in the zone with height $d1$ and thereafter in the zone with height $d2$. This means that in the zone $|z| < 0.5d2$, the cell dimensions are $\Delta x = 0.25\Delta x_0$, $\Delta y = 0.25\Delta y_0$ and $\Delta z = 0.25\Delta z_0$, where $(\Delta x_0, \Delta y_0, \Delta z_0)$ are the cell dimensions for $|z| > 0.5d1$. In the zone $0.5d2 < |z| < 0.5d1$, the cell dimensions are $\Delta x = 0.5\Delta x_0$, $\Delta y = 0.5\Delta y_0$ and $\Delta z = 0.5\Delta z_0$. The NWT is equipped with a numerical beach on the side opposite of the wavemaker to prevent wave reflections. The wavemaker at the NWT inlet is an “artificial” wavemaker represented by a numerical boundary condition, while the numerical beach uses a shallow-water absorption condition for which details can be found in, e.g., Higuera et al. [48]. The floater is placed at a distance $L1$ from the wavemaker and $L2 = L - L1$ from the numerical beach. The values of the parameters $d1$, $d2$, L and $L1$ are given in Table 8. In Table 8, λ refers to the wavelength associated with incident wave of wave period T and other variables as defined earlier in the text. The NWT size in y-direction is approximately $1.8B$, where $B = 51.8$ m (column centre-to-centre distance).

The complete set of boundary names for the NWT is shown in Figure 7 with boundary conditions specified in Table 9. Here, no-slip (zero velocity) boundary conditions are enforced at the seabed and on the floater hull, while a slip condition is enforced on the side wall, i.e., only the normal velocity is zero. At the top boundary (atmosphere), a constant total pressure condition of zero is applied. As the floater is symmetric about the xz plane through $y = 0$, only half of the floater and NWT are modelled with symmetry conditions enforced at $y = 0$. For moving boundaries, the deforming mesh (DM) method is applied with details described later.

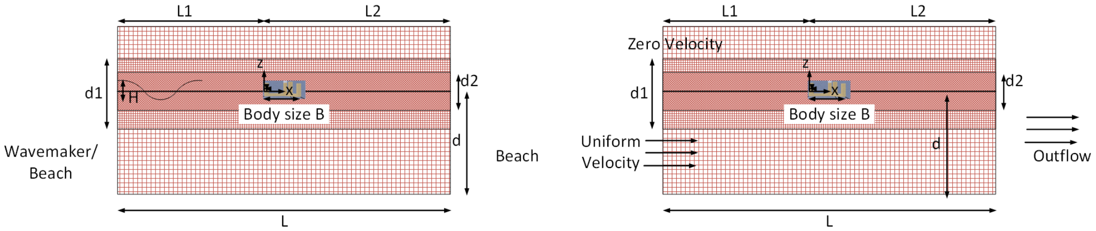

Figure 6. Boundary conditions for simulations with floater hull only. **Left**: Diffraction, forced motion and free decay cases. **Right**: Uniform current cases.

Table 8. NWT parameters for floater hull only cases.

Case/Case #	*d*1 (m)	*d*2 (m)	*T* (s)	T_f (s)	*U* (m/s)	*L* (m)	*L*1 (m)
Diffraction (1)	7.0–14.0H 7.0–14.0H	3.0–6.0H 3.0–6.0H	6, 8, 10 12	- -	- -	5.0 λ 4.0λ	2.0λ 1.0λ
Forced motion and Free decay (2, 3)	84.0A_f 21.0A_f	36.0A_f 9.0A_f	- -	10.0 15.0	- -	4.0B 4.0B	2.0B 2.0B
Uniform current (4)	$B/2.0$	$B/4.5$	-	-	1.0	3.0B	1.0B

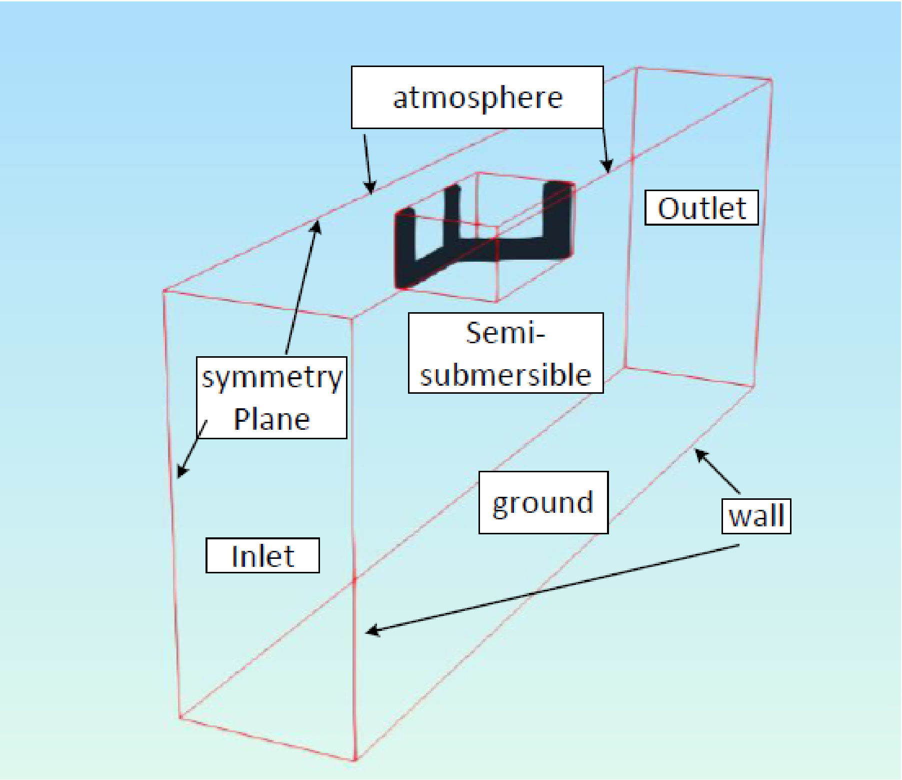

Figure 7. Boundary names for floater hull only cases.

Floater hull and rotor: A single-phase 3D air domain with uniform inflow is established for the case denoted as "case 5" (Figure 8), and a two-phase 3D NWT with two inlets and outlets for the air and wave fields (Figure 9) is established for the cases denoted as "case 6". For moving boundaries, i.e., the rotor and the floater hull, the overset grid (OG) method is used. In the OG method, a body-fitted overset grid follows the rigid motion of the solid boundary it is fitted to, moving over the fixed background grid without any mesh deformation. The dimensions of the OG and background grid are defined in Table 10 in terms of the model-scale body length b_M and the model-scale rotor diameter RD_M. The boundary names for the NWT are shown in Figures 8 and 9 with specification of the boundary conditions provided in Table 11. Due to the 3D nature of the considered flow, no symmetry plane is used. The inlet and outlet boundaries are divided into two parts for air and water, respectively. The air flow field at the inlet is represented by a uniform flow with constant velocity, the air pressure is set equal to atmospheric at the outlet, and the top boundary has a slip condition with zero normal velocity. The wave generation and absorption at the water inlet/outlet boundaries are similar as explained in connection with Table 9.

Table 9. Specification of boundary conditions for floater hull only cases.

Boundary Name	**Physical Representation**	**Enforced Conditions**
Diffraction cases		
Inlet	Wavemaker	Prescribed wave velocity
Outlet	Beach	Shallow-water absorption
Ground	Flat seabed	Zero total velocity
Wall	Slip	Zero normal velocity
Atmosphere	Atmospheric pressure	$P = p_{\text{atm}}$
symmetryPlane	Symmetry plane	-
Semi-submersible	Fixed body	Zero total velocity
Forced motion/free decay cases		
Inlet	Beach	Shallow-water absorption
Outlet	Beach	Shallow-water absorption
Ground	Flat seabed	Zero total velocity
Wall	Slip	Zero normal velocity
Atmosphere	Atmospheric pressure	$P = p_{\text{atm}}$
symmetryPlane	Symmetry plane	-
Semi-submersible	Prescribed/free body motion	Zero relative velocity
Uniform current cases		
Inlet	Uniform inflow	Prescribed velocity
Outlet	Uniform outflow	Mass flux outlet
Ground	Flat seabed	Total zero velocity
Wall	Slip	Normal velocity zero
Atmosphere	Atmospheric pressure	$P = p_{\text{atm}}$
symmetryPlane	Symmetry plane	-
Semi-submersible	Fixed body	Zero total velocity

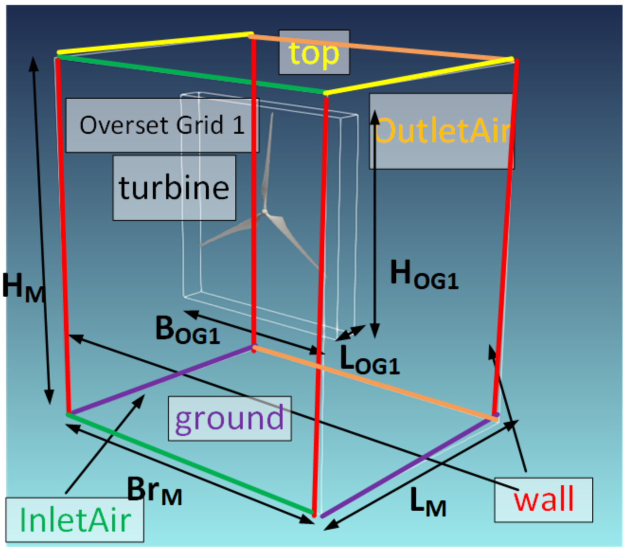

Figure 8. Boundary names for fixed rotor case.

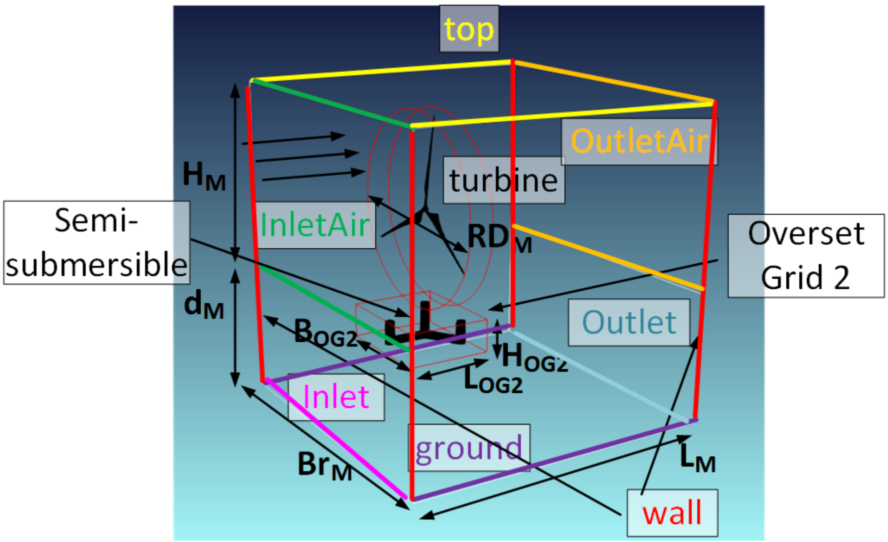

Figure 9. Boundary names for floater hull with rotor case.

Table 10. NWT parameters for floater hull and rotor cases, given in terms of b_M or RD_M, respectively, the model-scale body length and rotor diameter.

Case	L_M	H_M	Br_M	d_M	L_{OG1}	L_{OG2}	H_{OG1}	H_{OG2}	B_{OG1}	B_{OG2}
5	1.75 RD_M	1.35 RD_M	1.75 RD_M	-	0.15 b_M	-	1.5 RD_M	-	1.2 RD_M	-
6	″	″	″	1.67 b_M	″	1.3 b_M	″	0.55 b_M	″	1.7 b_M

Table 11. Specification of boundary conditions for floater hull and rotor cases.

Boundary Name	Physical Representation	Enforced Conditions
Fixed turbine (case 5)		
Inlet Air	Uniform inflow	Prescribed velocity
Outlet Air	Uniform pressure	$P = p_{\text{atm}}$
Inlet	-	-
Outlet	-	-
Ground	Flat seabed	Zero total velocity
Top	Slip	Zero normal velocity
Wall	Slip	Zero normal velocity
Turbine	Rotating blades	Prescribed angular velocity
Overset grid1	Interpolation between overset and background grid	-
Semi-submersible	-	-
Overset grid2	-	-
Rotating turbine with floater (cases 6)		
Inlet Air	Uniform inflow	Prescribed velocity
Outlet Air	Uniform pressure	$P = p_{\text{atm}}$
Inlet	Wavemaker	Prescribed wave velocity
Outlet	Beach	Shallow-water absorption
Ground	Flat seabed	Zero total velocity
Top	Slip	Zero normal velocity
Wall	Slip	Zero normal velocity
Turbine	Rotating blades	Prescribed angular velocity
Overset grid1	Interpolation between overset and background grid	-
Semi-submersible	Free body motion (in heave and pitch)	Zero relative velocity
Overset grid2	Interpolation between overset and background grid	-

4.2.3. Meshing in OpenFOAM

The numerical solution domain for velocity and pressure in OpenFOAM is defined through discretizing the fluid domain into cells. For simple body shapes and for general background meshes, a Cartesian structured hexahedral (*hex*) mesh can be generated using OpenFOAM's "blockMesh" utility. The overset grid fixed to the body (semi-submersible) surface is generated using OpenFOAM's "snappyHexMesh" utility, which refines cells near the body surface to account for local flow features associated with the body shape. For general bodies with arbitrary boundary shapes, such refinement cannot be performed using hexahedral cells alone, and requires the addition of prism/tetrahedral (*tet*) cells. This results in unstructured meshes, where an example of such "snapped" surface mesh is shown in Figure 10.

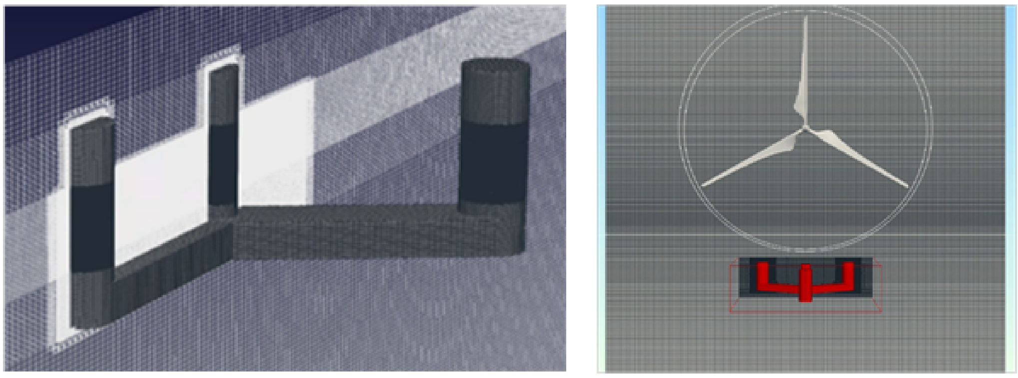

Figure 10. Body-surface mesh for hull (**left**) and overset grids (**right**) generated with the SnappyHexMesh utility.

For the diffraction, radiation/free decay and uniform current cases, a structured background mesh consisting of hex cells is established for the NWT with cell dimensions in three directions defined in Table 12. Windt et al. [49] has shown that 10–20 cells per wave height (CPH) in the free-surface region give accurate results for wave-propagation cases. For diffraction cases, a CPH value of 12–24 is used in zone d2 depending on the wave height H. For radiation/free decay and uniform current cases, a CPH value of 12 is used. SnappyHexMesh is then used to generate a refined mesh "snapped" around the floater hull. For cases 5–6, the mesh cell dimensions for the fixed background and moving overset grids are given in Tables 13 and 14. The mesh cell dimensions for OG1 is the same for both cases. Inside the overset grids a structured mesh for body surfaces is generated with SnappyHexMesh. For the rotor OG, 5 layers of prism cells (boundary layer cells) are used on the rotor surface, with a growth rate of 1.2. The thickness of first prism layer ($\delta OG1_p$) away from the blade surface is kept as 0.005 m; this implies that $c_{max}/\delta OG1_p = 40$, where c_{max} is the maximum chord of foil sections along the entire blade.

Table 12. NWT mesh properties for floater hull cases 1–4.

Diffraction Cases	T **(s)**	$B/\Delta x$	$B/\Delta y$	$H/\Delta z$	$H/\Delta z$ **(Zone** $d2$**)**
	6, 8, 10	25.90	41.44	3, 6	12, 24
	12	17.27	41.44	3, 6	12, 24
Forced Motion	T_f **(s)**	$B/\Delta x$	$B/\Delta y$	$A_f/\Delta z$	$H/\Delta z$ **(Zone** $d2$**)**
	10, 15	17.27	41.44	2, 4	12
Free Decay		$B/\Delta x$	$B/\Delta y$	$A_f/\Delta z$	$H/\Delta z$ **(Zone** $d2$**)**
		17.27	41.44	2, 4	12
Uniform Current		$B/\Delta x$	$B/\Delta y$	$A_f/\Delta z$	$H/\Delta z$ **(Zone** $d2$**)**
		17.27	41.44	2, 4	12

Table 13. NWT mesh properties for rotor case 5.

$L_M/\Delta x$	$Br_M/\Delta y$	$H_M/\Delta z$	$L_{OG1}/\Delta x$	$H_{OG1}/\Delta z$	$B_{OG1}/\Delta y$
200	150	250	30	75	75

Table 14. NWT mesh properties for floater hull and rotor case 6.

$L_M/\Delta x$	$Br_M/\Delta y$	$H_M/\Delta z$	$d_M/\Delta z$	$L_{OG1}/\Delta x$	$H_{OG1}/\Delta z$	$B_{OG1}/\Delta y$
200	150	400	200	120	62	100

4.2.4. Mesh Motion in OpenFOAM

In the present work, moving rigid bodies are assumed. The mesh motion in OpenFOAM is solved using an arbitrary Lagrangian Eulerian (ALE) formulation by two methods: deforming mesh (DM) and rigid body mesh motion. The overall mesh topology (cell umber and the connection to neighbours) is retained in both techniques.

In the DM method, the cells deform when the instantaneous position of the body changes. For reference, comprehensive analysis of DM techniques and respective implementation in OF is given by Jasak and Tukovic [50]. In the present work, the "laplacianDisplacement" solver is selected for implementation of the DM method, where the mesh deformation depends on the body motion. The mesh motion is solved using an additional Laplace equation. This equation is given as $\Delta(k_d \vec{d}) = 0$, where k_d is a diffusivity coefficient with $\vec{d}$ being the displacement vector of each cell centre. A quadratic diffusivity coefficient k_d given as r^2 is employed, where r is the minimum distance between the cell and the specified moving boundary. This choice of diffusivity coefficient implies that as we move away from the body boundaries, the deformation decreases. The DM method is here implemented for cases with forced motions and free-decay heave motions.

In the rigid mesh motion technique, the mesh moves with the body without deforming. This is applied in the OG method where overset meshes are applied. Here, two grids are considered, namely a (generally structured) background mesh over the entire domain, and a smaller overset mesh which is fitted to the body and covering a small region around the body. The background grid remains fixed, whereas the overset mesh follows the rigid-body motion without any distortion. The governing fluid-flow equations are solved for each mesh, and the physical quantities are coupled for the two meshes using interpolation schemes. Information is exchanged between the meshes at two single-celled layers: One for the background mesh close to and including the body boundary and the other for the body-fitted overset mesh at its outermost cell layer. In the former layer, information is exchanged from the body-fitted overset mesh to the background mesh, whereas in the latter layer, information is exchanged in the other direction. The overset mesh is boundary fitted, meaning that the region occupied by the body is not populated with cells. In the background mesh, however, cells exist also inside the body. Such cells are denoted as "hole" cells and there, no fluid equations are solved. An example of the "interpolation" layer and "hole" region is shown in Figure 11. The OG method is implemented in simulation cases 5–6.

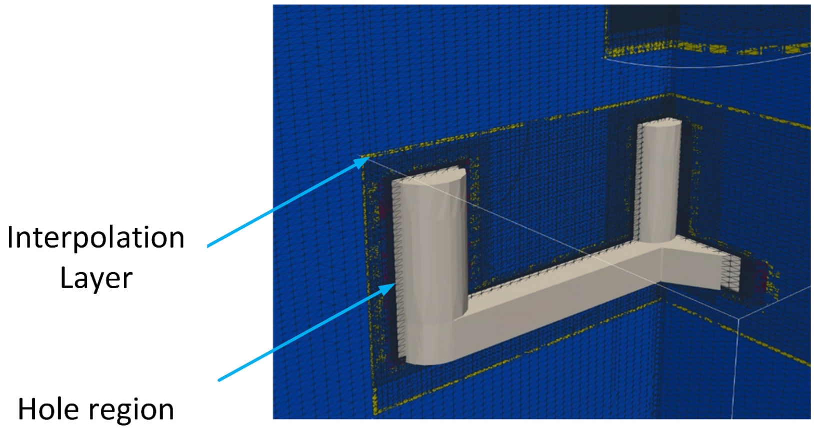

Figure 11. Screenshot showing interpolation and hole regions in the OG method.

5. Data Analysis

This section describes methods for extracting physical quantities of interest using the data obtained from the PF and CFD simulations.

5.1. Potential Flow Solver

The added mass and damping along with transfer functions for first-order wave loads and mean second-order wave drift loads are obtained directly as function of wave frequency from WADAM and can be compared directly with CFD results for specific wave or forcing periods. Based on the frequency domain solution from WADAM, Orcaflex computes the hydrodynamic loads in time domain and then solves the coupled aero-hydrodynamic problem. Results such as aerodynamic thrust, motions of the floater hull and RNA, etc., are available as time series upon a successful time domain simulation and can be directly compared with results from CFD simulations.

5.2. CFD Solver

For the CFD solver, data must be post-processed to obtain results that can be compared with the PF solver. For the cases where direct time-series comparison is not possible, the methods used to extract the relevant quantities of interest are described below.

5.2.1. Diffraction Cases

To examine the wave generation, propagation and absorption capabilities of the established NWT, regular waves are generated for all wave periods (given in Table 5) without the presence of the floater using Stokes second-order wave theory with the free-surface elevation measured in a wave probe (WP1) placed at the origin of the tank ($L1$ distance from the wavemaker). An example for T = 12 s and H = 3 m is shown in Figure 12. Compared with a theoretical Stokes second-order solution, the waves generated in OF are in good agreement for all periods considered (difference less than 5%). The largest error occurs for T = 6 s and H = 6 m, indicating that second-order theory may be insufficient to capture the wave nonlinearity due to large wave steepness for this particular condition. A steady-state time window of 4–8 T is available for all wave periods where reflection from the numerical beach does not affect the free-surface elevation in the location of WP1 (where the floater is located in subsequent simulations). The mean wave height H in WP1 for this steady-state time interval (without the floater present) determines the wave amplitude, $A = H/2$, used to estimate wave-load transfer functions when the analyses are re-run with the floater present.

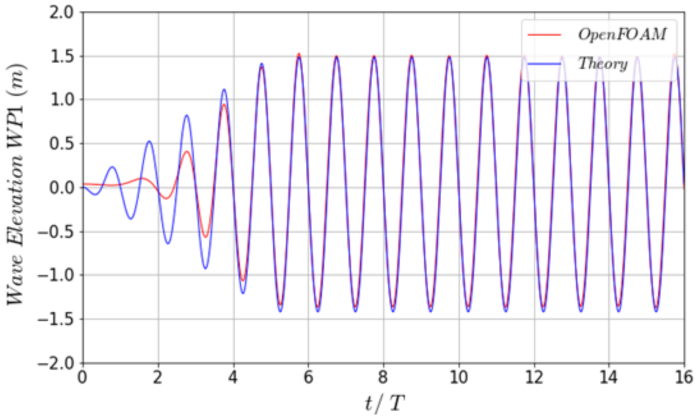

Figure 12. Wave elevation for T = 12 s and H = 3 m compared with the Stokes second-order theory.

In Siddiqui et al. [40], the focus was on mean wave drift loads, whereas we here focus on first-order wave loads. Figure 13 shows the time series of the surge force (F_x) from OF for 0° wave heading, T = 12 s and H = 3 m. A steady-state range from the force time series (shown in blue in Figure 13) is used to estimate the first-order force F_{1xA}. The steady-state range generally consists of n oscillation periods, where n is an integer number between 3 and 5 depending on the wave period T, and is taken such that the effect of reflection from the beach and the wavemaker is minimal. F_{1xA} for surge (and F_{1zA} for heave) is calculated by taking the average of the crest (F_{Ac}) and trough (F_{At}) values in the time series over the steady-state time window nT, i.e.,

$$F_{1xA} = \frac{\sum_{j=1}^{j=n} (|F_{Ac}| + |F_{At}|)}{2n} \tag{1}$$

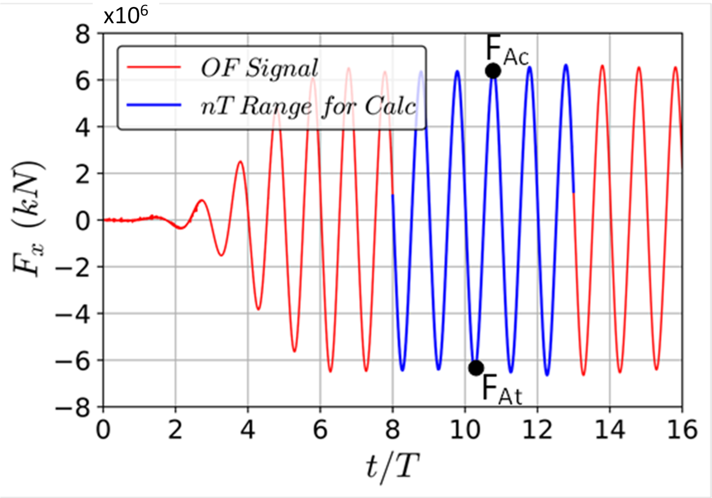

Figure 13. Surge force (F_x) from OF for T = 12 s and H = 3 m.

5.2.2. Added Mass and Damping Coefficients

For radiation (forced motion) simulations, the method described in Journee and Massie [51] is used to estimate frequency-dependent added mass a_{kj} and damping coefficients b_{kj}:

$$a_{kj} = \frac{c_{kj} - \frac{F_{kjA}}{\eta_{jA}} cos(\epsilon)}{\omega^2} \tag{2}$$

$$b_{kj} = \frac{F_{kjA} sin(\epsilon)}{\omega \eta_{jA}}. \tag{3}$$

Here, $F_{kj}(t) = F_{kjA} sin(\omega t + \epsilon)$ is the hydrodynamic force in direction k due to forced motion $\eta_j(t) = \eta_{jA} sin(\omega t)$ in direction j, ω is the forcing frequency, c_{kj} is the hydrostatic restoring coefficient, and ϵ is the phase difference between the force $F_{kj}(t)$ and motion $\eta_j(t)$.

5.2.3. Free Decay Tests

The damping from the free decay cases is calculated using the logarithmic decrement method described in detail by Faltinsen [52].

5.2.4. Uniform Current, Fixed, and Floating Turbine Forces

For these cases, force time series obtained directly from the simulations are evaluated.

6. Results and Discussion

Results for the cases described in Section 3 are here discussed in detail.

6.1. First-Order Wave Frequency Loads and Second-Order Mean Wave Drift Loads

We consider transfer functions for the first-order forces in surge and heave on the fixed floater at two wave heights (H = 3 m and 6 m), two wave headings (0°, 180°), and two mean pitch angles (0°, 5°) from PF and CFD displayed in Figure 14. The forces in surge from CFD are generally in fair agreement with PF results. Nonlinearity in the surge force from CFD can be seen for T = 6 s where there is a notable difference between H = 3 m and 6 m, but is less apparent for other wave periods. It is plausible that this observation may be related to wave steepness and nonlinearity of the incident waves, since the smaller wave periods are associated with larger steepness. The effect of adding a mean pitch angle to the floater is generally small, but slightly more notable for the heave force than for the surge force. The largest difference for both degrees of freedom occurs for the second smallest wave period examined. Although not reported here, the effect of adding a non-zero pitch angle is insignificant in the (linear) PF analysis. The fact that the CFD analysis shows a visible difference suggests that the effect of a non-zero mean pitch is primarily of nonlinear nature. Additionally, the CFD results on average display a somewhat larger difference between results for the two wave directions from PF, which is possibly related to viscous effects.

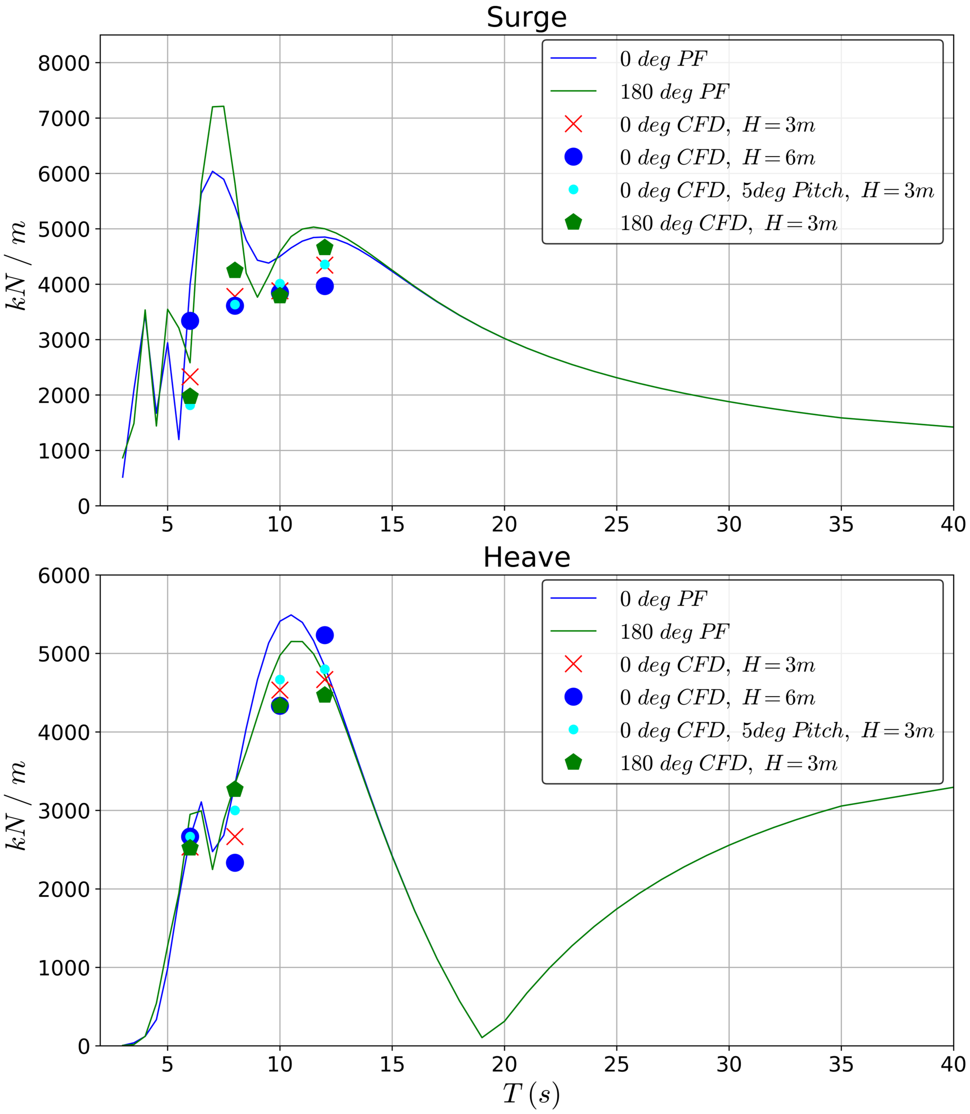

Figure 14. Comparison of first-order wave loads in surge and heave in PF and CFD.

Results for mean wave drift loads were discussed in Siddiqui et al. [40] with main findings briefly summarized below:

- There are considerable differences between CFD results and PF results, even when the empirical formula for viscous-flow corrections (ExWave) proposed in Yang et al. [53] are included in the latter. The difference increases for large wave periods and wave heights. This may be of significance for analysis of FOWT systems with hulls consisting of slender members, and should be further studied;

- Adding a non-zero mean pitch angle shows little influence on the PF results but is more visible in the CFD results. The exact reason for this difference and the underlying physics need further examination.

6.2. Added Mass and Damping Coefficients

6.2.1. Forced Oscillatory Motions

Figure 15 compares the added mass and radiation damping coefficients calculated from CFD harmonic motions and from PF, where the CFD simulations were performed for two amplitudes and three forcing periods each. The added mass in heave and added inertia in pitch from CFD are in fair agreement with PF, whereas the damping coefficients from CFD are larger than from PF. The latter can possibly be explained by viscous effects, which is not accounted for in the PF results.

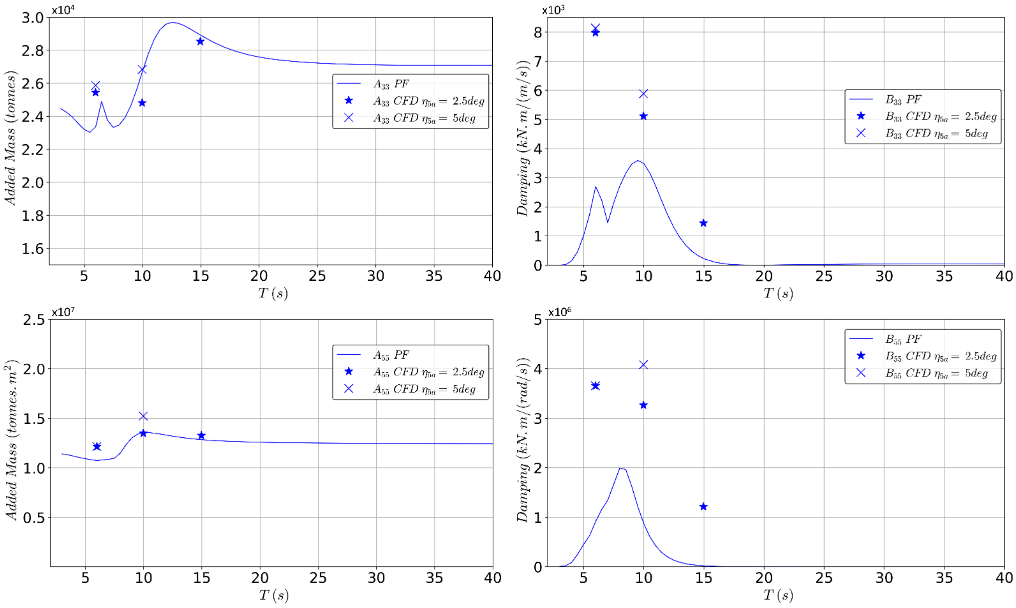

Figure 15. Comparison of added mass (**left**) and damping (**right**) in heave (**top**) and pitch (**bottom**) motions estimated with PF and CFD.

The significance of viscous effects in the CFD results is further indicated by the nonlinearity for T_f = 10 s, observed as difference in coefficients for different forcing amplitudes. Figure 16 shows the CFD velocity field at two different time instants during forced heave motion for this forcing period. Significant differences are observed in the flow field during downward (left plot) and upward motion of the hull (right plot), where one may notice the formation of positive vortices during downward motion and negative vortices during upward motion. These vortices contribute to additional viscous damping in heave, and a similar phenomenon is observed during forced pitch motions.

Each combination of forcing period and amplitude in the forced-motion CFD analysis takes around 10–15 h of CPU time. By comparison, computing results in frequency domain for all 75 wave periods with the PF solver takes less than 30 min of CPU time.

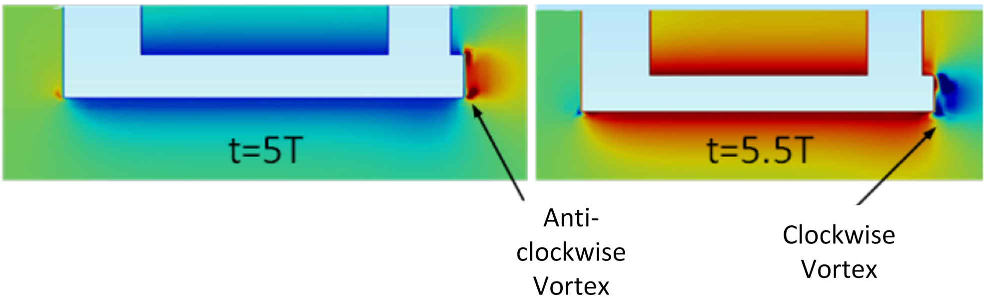

Figure 16. Screenshots at two different time instants showing the velocity field in a xz cut-plane for forced heave motions from CFD simulations for T_f = 10 s and η_{3a} = 0.5 m.

6.2.2. Free Decay Simulations

Figure 17 shows the comparison of free decay heave motion with an initial amplitude of 1.5 m from PF and CFD. The PF method here refers to time domain simulations in Orcaflex, where quadratic damping is represented using a Morison element (ME) model (shown in Figure 18) with generic drag coefficients defined in Table 15. It is seen that the natural heave period is in good agreement between the two methods, whereas the CFD results indicate slightly larger damping than the PF results. The estimated natural periods and damping coefficients from the decay test are listed in Table 16, indicating that both linear and quadratic damping are larger in the CFD simulations. The results in this section therefore demonstrate that by performing decay tests in CFD, a PF model can potentially be calibrated to achieve a more accurate damping level than by using generic drag coefficients. Alternatively, a PF model may be calibrated against experimental decay tests. Performing a hydrodynamic model test is however usually more expensive and time consuming than performing free-decay CFD simulations, which in this case took around 15 h for one decay test. In addition, model test results may be influenced by improper scaling of viscous effects. The reason for why calibrating a PF model may lead to improved damping accuracy over using generic coefficient is partly due to hydrodynamic interaction effects: although generic coefficients may represent the drag load on a single structural member well in isolation, there is uncertainty related to, e.g., shielding effects behind "upstream" columns.

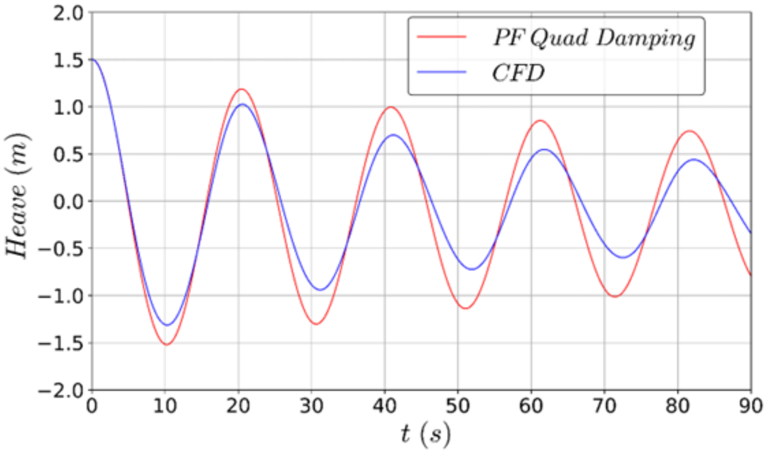

Figure 17. Comparison of free decay heave motion from PF (including quadratic damping from empirical formula) and CFD.

Table 15. Drag coefficients for Morison elements (based on DNV [54]).

	C_{Dx}	C_{Dz}
Columns	1.0	1.0
Pontoons	2.3	1.4

Table 16. Natural period and linear and quadratic damping in heave from free decay tests.

	T_{n3} (s)	B_{33L} (kNs/m)	B_{33Q} (kNs^2/m^2)
PF	20.40	33.68	463.32
CFD	20.54	143.77	776.73

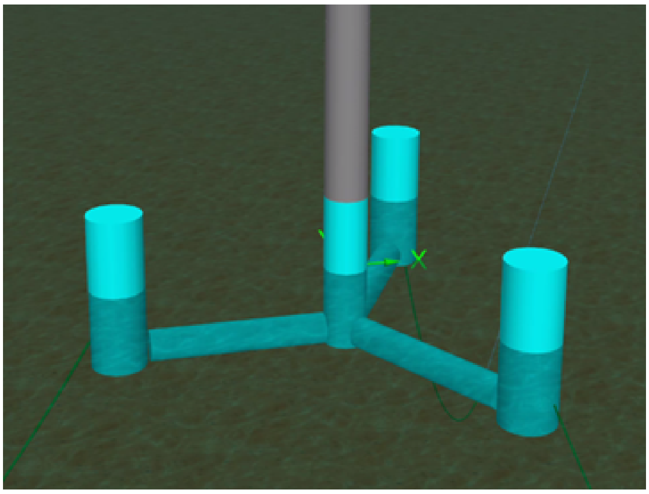

Figure 18. ME representation of floater hull in Orcaflex model.

6.2.3. Drag Force in Uniform Current

The ME formulation described earlier (with coefficients defined in Table 15) is used in the PF solver to estimate drag loads in uniform current. Since the drag coefficients in the PF solver are generic and do not account for shielding effects, they give the same total drag force in x-direction for both 0° and 180° current directions. The resulting drag forces from PF and CFD with a uniform current velocity of 1 m/s are compared in Figure 19, where one may observe that the mean value in the CFD simulations for 0° current direction (after the initial transient) is close to the PF value. However, the CFD simulation gives a significantly smaller drag force than the PF results for 180°. Evidently, the drag force takes some time to converge towards steady state in the CFD simulations. This is also seen in the snapshots in Figure 20, demonstrating how the flow field around the floater develops over time. Far from the body and close to the walls, a uniform velocity of 1 m/s (coinciding with the incoming current velocity field) is seen, indicating that the size of the computational domain is sufficient. In regions close to the floater columns, there are pockets of lower and higher velocities, and a strong interaction between the central column and the side columns can be observed. The fact that the hydrodynamic interaction between the central and side columns interests the upstream flow region for 180° heading and the downstream region for 0° heading is likely a major reason for the less satisfactory agreement between CFD and PF for current direction 180° than for 0°.

The influence on shielding and hydrodynamic interaction effects, as well as 3D flow features at the connections between columns and pontoons, should be further investigated in future work.

For the uniform current simulations presented here, the CFD solver takes about 5–10 h of CPU time compared to 2 min for the PF solver.

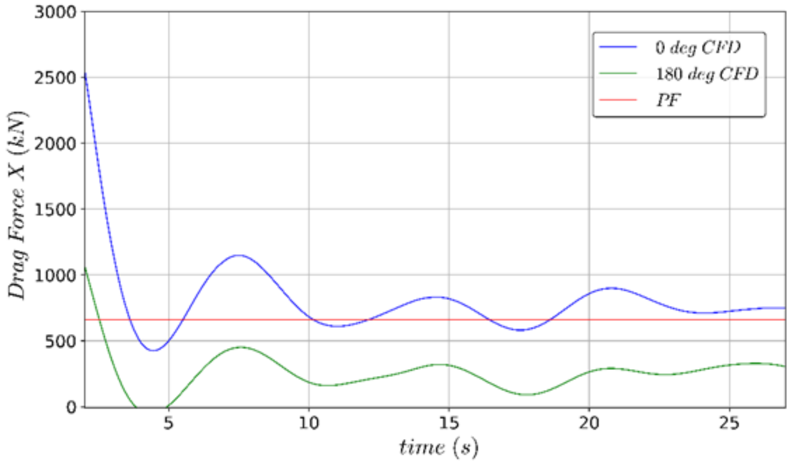

Figure 19. Comparison of drag forces in x-direction from PF and CFD.

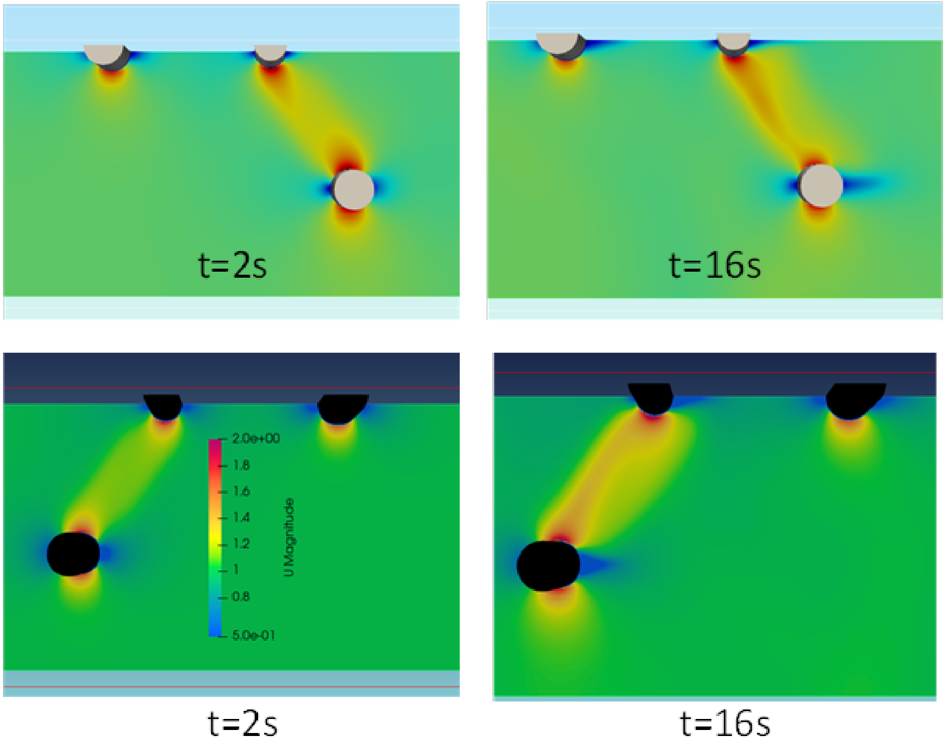

Figure 20. Snapshots of velocity field from CFD simulations in a xy cut plane at two different time instants for 0° (**top**) and 180° (**bottom**) current directions.

6.2.4. Fixed and Floating Turbine

PF simulations have been performed for the fixed down-scaled turbine without the tower in Orcaflex with rigid turbine blades. Similarly, a CFD simulation was performed for the fixed turbine using the OG method for the rotating turbine. An inflow wind velocity of U_W = 1.2 m/s and an angular turbine rotation velocity of 6.13 rad/s for the turbine was used in both solvers. The simulation time was restricted to 2 s due to excessive CPU time required by the CFD simulation. However, it is recognized that a longer run time is required to ensure steady-state conditions. Figure 21 shows the comparison of the aerodynamic thrust force in x-direction between the two solvers. There is an initial transient in the CFD time history, but it converges against steady-state condition near the end of the simulation with a mean value around 6.5 N. The results from both solvers are compared against experimental results from Kimball et al. [38] to validate the simulation setup for both solvers. The CFD solver thrust is around 6.2% larger than the experimental result while the PF solver gives a values around 12.7% larger. Based on this, both solvers are deemed to provide reasonable thrust forces. Different from the PF solver, the CFD solver also provides information about the flow field around and behind the turbine (wake region). Such information can be important for turbine interaction analysis in a wind farm and blade design. Further discussion about the wake behind the fixed turbine is discussed in relation with the floating turbine later.

For these 2 s of simulation, the CFD solver took about 2.5 days of CPU time compared to approximately 10 s for the PF simulation.

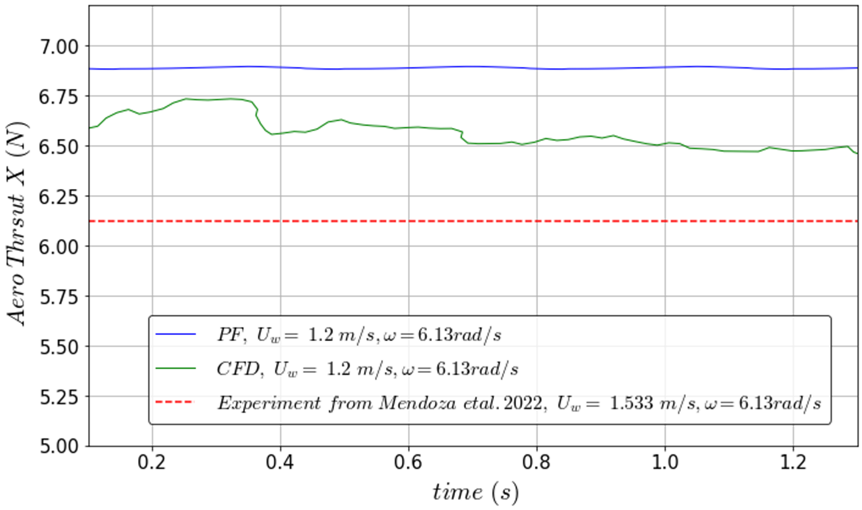

Figure 21. Comparison of aerodynamic thrust force in the x-direction between PF and CFD for fixed turbine with wind velocity U_{WM} = 1.2 m/s and turbine blade rotation angular velocity 6.13 rad/s.

PF and CFD simulations were also performed for the floating down-scaled turbine and floater with a uniform wind velocity of U_{WM} = 1.2 m/s, incident wave height H = 0.071 m, and wave period T = 0.7 s. A ramp function for the wave generation and turbine rotation was implemented for in solvers with a ramp-up time of 0.1 s. The PF setup in Orcaflex is shown in Figure 22, while snapshots of two different time instants from the CFD simulation are shown in Figure 23.

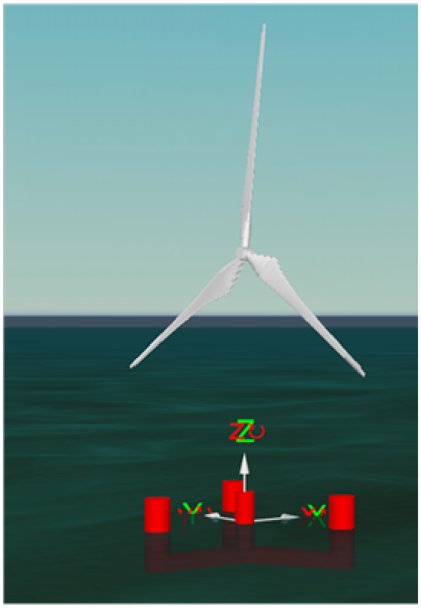

Figure 22. Setup of the scaled wind turbine along with the floater in Orcaflex.

A simulation time of 2.8 s (4 wave periods) was used, where the CFD simulation was terminated due to excessive CPU time. However, the simulations should strictly speaking have been run longer to reach steady-state behaviour. The aerodynamic thrust for the two solvers is compared in Figure 24. The difference in mean thrust (around 33% relative to PF) is larger between the PF and CFD solvers for the floating turbine compared to the fixed turbine discussed previously. However, longer simulations must be investigated as part of future work to conclude on this aspect. No experimental data was available for this case.

For these simulations, the CFD solver took around 7 days of CPU time compared to 5 s for the PF solver.

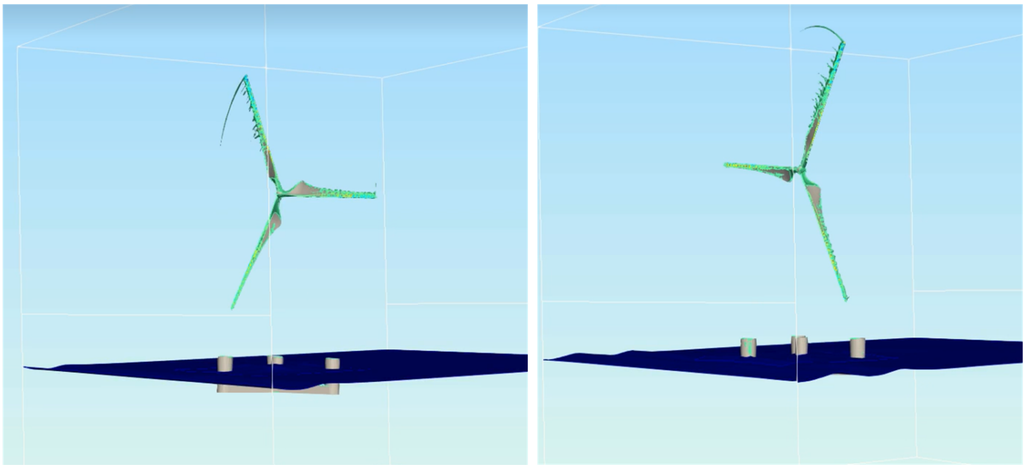

Figure 23. Snapshots from two different time instants from simulation of the scaled wind turbine along with the floater in CFD.

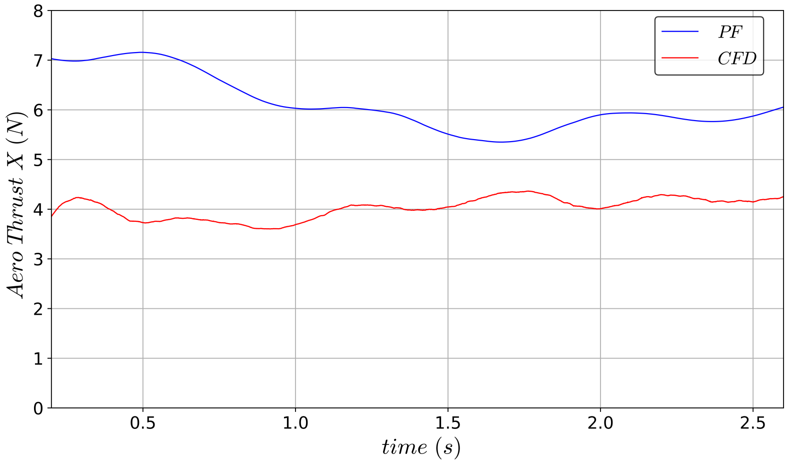

Figure 24. Comparison of aerodynamic thrust force in x-direction between PF and CFD for floating turbine.

One of the subsequent aims mentioned in the present work was to understand the flow behind the floating turbine blades (wake region), which cannot be described by the PF solver. Such a study can help in operational aspects and understanding optimal FOWT locations within a wind farm. Figure 25 demonstrates the velocity field behind the floating turbine in a xy plane section for three different time instants. The xy section is through a cut with z = 1.941 m (centre of the rotor hub). As the CFD simulations are run for a relatively short simulation time, it is not possible to comment on the wake features in intricate detail (as has been done in some of the mentioned literature here). However, the main aim is to demonstrate that the velocity field can indeed be captured well for a CFD solver and can be an important tool to understand how far the wake region extends behind the turbine before reaching ambient velocity levels, and subsequently how the wake affects the other turbines downstream in a FOWT farm. The present work represents a starting point towards such a study. Future work should be performed with larger simulation times along with a study towards influence of turbulent-flow effects in the wake features.

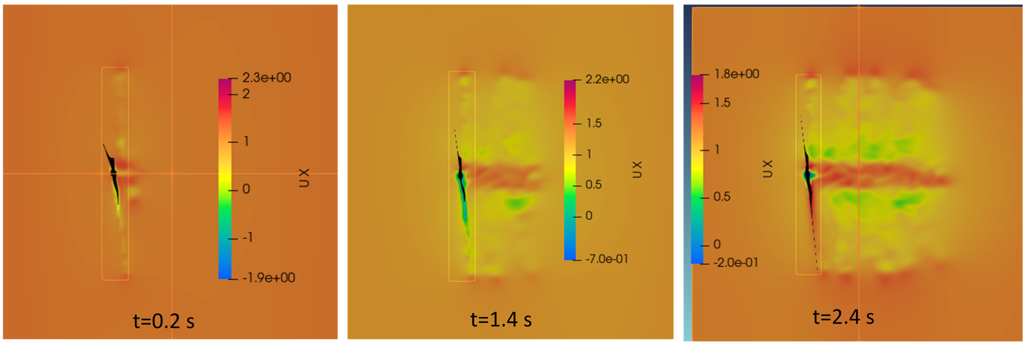

Figure 25. Snapshots of the velocity field in a xy plane section (cut with z = 1.941 m) at three different time instants from the floating-turbine CFD simulation.

7. Conclusions

The aim of the present work was to investigate the usefulness of CFD in the analysis of FOWTs by comparing CFD results from OpenFOAM with PF results from Orcaflex. The former properly accounts for nonlinear hydrodynamics including viscous-flow effects, whereas the latter uses hydrodynamic coefficients from a frequency domain analysis based on perturbation theory combined with empirical formulations for viscous-flow effects. A 15 MW open-source turbine with an associated floater, mirroring the industry trend of going towards larger turbines, are used as basis for the study together with relevant environmental parameters. To avoid excessive computational demands, scaled versions of the turbine and floater were modelled in the CFD setup. However, a full-scale floater was modelled for pure hydrodynamic cases. Details for the boundary conditions, mesh generation, and solver setup are thoroughly explained. The following observations are highlighted from the comparison between CFD and PF:

- Hydrodynamic coefficients estimated with PF and CFD generally agree well. However, some nonlinear behaviour not captured in the PF results are indicated by the CFD method. For diffraction scenarios, the CFD results indicate instances of moderate nonlinearity related to increasing wave steepness and mean floater pitch, and for the mean wave-drift forces, the CFD results indicate some nonlinearity related to increasing wave height (documented in Siddiqui et al. [40]);
- Added mass coefficients from forced oscillation CFD simulations are in fair agreement with PF results. The damping forces due to forced oscillations in the CFD simulations are on the other hand significantly larger than the PF radiation damping. This is attributed to rotational and viscous-flow effects. For a direct comparison between CFD and PF radiation damping, CFD simulations should ideally have been performed without viscosity. Nevertheless, the results indicate that viscous damping must be added in PF, preferably calibrated against CFD or experiments, to yield physically sound behaviour. This is here exemplified through a comparison of free-decay CFD and PF simulations;
- In uniform current, the drag force obtained with the CFD solver shows a directional dependence that cannot be reproduced by using Morison elements in the PF solver. This is due to viscous directional dependent interaction effects between the columns that may be important to account for to reliably estimate hydrodynamic loads due to current and/or waves, or resistance during towing. In this regard, the use of CFD may help to capture flow physics not revealed by PF at a reasonable computational cost (as a moderate simulation time is needed to estimate loads in uniform compared to unsteady inflow). Such information may, e.g., be used to enhance the accuracy

of a PF model by introducing different Morison drag coefficients depending on the flow direction.

- The aerodynamic thrust forces obtained from the PF and CFD solvers are in good agreement for the fixed turbine case with differences less than 6%. However, for the floating turbine a significant difference (around 33%) is observed for reasons that should be examined in a future work.

To quantify the experiences made in the present work, Table 17 presents a cost-benefit analysis for the simulations performed considering four parameters: CPU time, setup complexity, potential advantages, and software license cost. The parameters are classified as "low", "medium", and "high" with points assigned from 1 to 3 to each depending on the parameter. For example, a "high" potential advantage corresponds to 3 points, whereas a "high" license cost corresponds to 1 point.

Table 17. Cost-benefit analysis for the simulations in the present work for PF and CFD solvers.

Solver	**CPU Time (s)**	**Setup Complexity**	**Potential Advantages**	**License Cost**	**Total (Max. 12)**
			Diffraction cases		
CFD	54,000–90,000 (Medium)	Medium	May provide more accurate description of forces for some scenarios (Low)	Low (open-source)	8
PF	1200–1800 (Low)	Medium	Reliable and efficient force calculation (Medium)	Medium	9
			Forced motion/free decay/Uniform current cases		
CFD	36,000–54,000 (Medium)	Medium	Detailed flow information in addition to forces. Realistic estimation of damping (High)	Low	9
PF	1200–1800 (Low)	Medium	Low	Medium	8
			Fixed turbine simulations		
CFD	216,000 (High)	High	Provides flow field information and may aid in blade design, in addition to force etc. (Medium)	Low	7
PF	10 (Low)	Medium	Allows implementation of flexible blades, controller (Medium)	Medium	9
			Floating turbine simulations		
CFD	604,800 (High)	High	Provides flow field information in addition to force etc., optimum turbine placing (Medium)	Low	7
PF	1300–1900 (Low)	Medium	Allows implementation of flexible blades, controller (Medium)	Medium	9

The cost-benefit analysis in Table 17 indicates that, in general, available industrial PF tools provide as good (if not better) results as the CFD solver while incurring significantly lower computational costs. When looking specifically towards analysis of hydrodynamic properties, on the other hand, the CFD solver has equal or better rating than the PF solver. This is, e.g., due to a more accurate representation of viscous damping. Although the computational cost of CFD for pure hydrodynamic studies is significantly larger than for PF, it is still considered reasonable.

The computational cost of performing coupled aero-hydrodynamic simulations with CFD is too high to justify the use of CFD for general analysis of floater motions, turbine thrust, etc. In addition, implementation of the controller and flexible blades in the CFD solver is needed, whereas state-of-the-art PF methods already have such capabilities built in. CFD does however present the opportunity to investigate the detailed flow patterns in downstream aerodynamic wakes, which can have utility in the overall design of a wind farm.

The main conclusion from the work is therefore that, considering the present state-of-the-art, available industrial PF tools are preferable for coupled aero-hydrodynamic simulations of FOWTs. CFD may however be a useful tool to improve the accuracy of hydrodynamic coefficients in PF models through calibration, and may in some cases be considered as an alternative to performing hydrodynamic model tests.

Author Contributions: Conceptualization, M.A.S., F.-C.W.H. and M.G.; methodology, M.A.S., F.-C.W.H. and M.G.; software, M.A.S. and F.-C.W.H.; formal analysis, M.A.S. and E.A.; writing—original draft preparation, M.A.S.; writing—review and editing, M.A.S., F.-C.W.H. and M.G.; supervision, F.-C.W.H. and M.G.; project administration, F.-C.W.H.; funding acquisition, F.-C.W.H. All authors have read and agreed to the published version of the manuscript.

Funding: This research was funded by RFF VIKEN project number 330675. One of the co-authors is connected with the Centre of Excellence NTNU AMOS, supported by the Research Council of Norway through the Centre of Excellence funding scheme AMOS, project number 223254. In addition, some of the simulations were performed on resources provided by UNINETT Sigma2—the National Infrastructure for High Performance Computing and Data Storage in Norway.

Data Availability Statement: Data are contained within the article.

Conflicts of Interest: Authors Mohd Atif Siddiqui and Finn-Christian Wickmann Hanssen were employed by Semar AS. The remaining authors declare that the research was conducted in the absence of any commercial or financial relationships that could be construed as a potential conflict of interest.

Abbreviations

The following abbreviations are used in this manuscript:

2D	two-dimensional
3D	three-dimensional
ALE	Arbitrary Lagrangian–Eulerian
BEM	Boundary Element Method
BEMO	Blade Element Momentum
CFD	Computational Fluid Dynamics
CFM	Conservation of fluid momentum
Co	Courant Number
DPI	Direct Pressure Integration
FOWT	Floating offshore wind turbine
FVM	Finite Volume Method
IEA	International Energy Agency
ME	Morison Element
MULES	Multidimensional Universal Limiter with Explicit Solution
NWT	Numerical Wave tank
OF	OpenFOAM
PF	Potential Flow
PISO	Pressure Implicit with Splitting of Operator
PLIC	Piecewise-Linear Interface Calculation
QTF	Quadratic Transfer Function
RNA	Rotor nacelle assembly
SIMPLE	Semi-Implicit Method for Pressure-Linked Equations
TLP	Tension Leg Platform
VOF	Volume of fluid

References

1. Matha, D.; Schlipf, M. Challenges in Simulation of Aerodynamics, Hydrodynamics, and Mooring-Line Dynamics of Floating Offshore Wind Turbines. In Proceedings of the 21st International Offshore and Polar Engineering Conference, Maui, HI, USA, 19–24 June 2011.
2. Otter, A.; Murphy, J.; Pakrashi, V.; Robertson, A.; Desmond, C. A review of modelling techniques for floating offshore wind turbines. *Wind Energy* **2022**, *25*, 831–857. [CrossRef]
3. NREL. FAST. 2021. Available online: https://www.nrel.gov/wind/nwtc/fast.html (accessed on 21 December 2021).
4. Orcina. Orcaflex. 2020. Available online: https://www.orcina.com/webhelp/OrcaFlex/Default.htm (accessed on 21 December 2021).
5. Dagher, H.; Viselli, A.; Goupee, A.; Thaler, J.; Brady, D.; Browne, P.; Browning, J.; Chung, J.; Coulling, A.; Deese, H.; et al. *Final Technical Report. DeepCwind Consortium Research Program. 15 January 2010–31 March 2013*; U.S. Department of Energy Office of Scientific and Technical Information: Oak Ridge, TN, USA, 2013. [CrossRef]

6. Stewart, G.M.; Lackner, M.A.; Robertson, A.; Jonkman, J.; Goupee, A.J. Calibration And Validation of a FAST Floating Wind Turbine Model of the DeepCwind Scaled Tension-Leg Platform. In Proceedings of the International Ocean and Polar Engineering Conference, Rhodes, Greece, 17–23 June 2012; p. ISOPE-I-12-033. Available online: https://onepetro.org/ISOPEIOPEC/proceedings-pdf/ISOPE12/All-ISOPE12/ISOPE-I-12-033/1604282/isope-i-12-033.pdf (accessed on 15 January 2022).
7. Wang, H.; Hu, Z.Q.; Meng, X.Y. Dynamic performance investigation of a spar-type floating wind turbine under different sea conditions. *China Ocean Eng.* **2018**, *32*, 256–265. [CrossRef]
8. Kim, J.; Shin, H. Validation of a 750 kW semi-submersible floating offshore wind turbine numerical model with model test data, part II: Model-II. *Int. J. Nav. Archit. Ocean. Eng.* **2020**, *12*, 213–225. . [CrossRef]
9. Ahn, H.; Shin, H. Experimental and Numerical Analysis of a 10 MW Floating Offshore Wind Turbine in Regular Waves. *Energies* **2020**, *13*, 2608. [CrossRef]
10. Thomsen, J.; Bergua, R.; Jonkman, J.; Robertson, A.; Mendoza, N.; Brown, C.; Galinos, C.; Stiesdal, H. Modeling the TetraSpar Floating Offshore Wind Turbine Foundation as a Flexible Structure in OrcaFlex and OpenFAST. *Energies* **2021**, *14*, 7866. [CrossRef]
11. Vittori, F.; Azcona, J.; Eguinoa, I.; Pires, O.; Rodríguez, A.; Morató, A.; Garrido, C.; Desmond, C. Model tests of a 10 MW semi-submersible floating wind turbine under waves and wind using hybrid method to integrate the rotor thrust and moments. *Wind Energ. Sci.* **2022**, *7*, 2149–2161. [CrossRef]
12. Sanderse, B.; van der Pijl, S.; Koren, B. Review of Computational Fluid Dynamics for Wind Turbine Wake Aerodynamics. *Wind Energy* **2011**, *14*, 799–819. [CrossRef]
13. Tossas, L.; Leonardi, S. *Wind Turbine Modeling for Computational Fluid Dynamics*; Subcontract Report NREL/SR-5000-55054; U.S. Department of Energy Office of Scientific and Technical Information: Oak Ridge, TN, USA, 2013.
14. Stergiannis, N.; Lacor, C.; Beeck, J.; Donnelly, R. CFD modelling approaches against single wind turbine wake measurements using RANS. *J. Phys. Conf. Ser.* **2016**, *753*. [CrossRef]
15. Beyer, F.; Arnold, M.; Cheng, P. Analysis of floating offshore wind turbine hydrodynamics using coupled CFD and multibody methods. In Proceedings of the International Ocean and Polar Engineering Conference, Anchorage, AL, USA, 30 June–5 July 2013; p. ISOPE-I-13-071.
16. Benitz, M.A.; Schmidt, D.P.; Lackner, M.A.; Stewart, G.M.; Jonkman, J.; Robertson, A. Comparison of Hydrodynamic Load Predictions Between Reduced Order Engineering Models and Computational Fluid Dynamics for the OC4-DeepCwind Semi-Submersible. In *Volume 9B: Ocean Renewable Energy, Proceedings of the International Conference on Offshore Mechanics and Arctic Engineering*; American Society of Mechanical Engineers: New York, NY, USA, 2014; p. V09BT09A006. Available online: https://asmedigitalcollection.asme.org/OMAE/proceedings-pdf/OMAE2014/45547/V09BT09A006/4432791/v09bt09a006-omae2014-23985.pdf (accessed on 15 January 2022). [CrossRef]
17. Benitz, M.A.; Schmidt, D.P.; Lackner, M.A.; Stewart, G.M.; Jonkman, J.; Robertson, A. Validation of Hydrodynamic Load Models Using CFD for the OC4-DeepCwind Semisubmersible. In Volume 9: Ocean Renewable Energy, Proceedings of the International Conference on Offshore Mechanics and Arctic Engineering; American Society of Mechanical Engineers: New York, NY, USA, 2015; p. V009T09A037. Available online: https://asmedigitalcollection.asme.org/OMAE/proceedings-pdf/OMAE2015/56574/V009T09A037/4435019/v009t09a037-omae2015-41045.pdf (accessed on 20 January 2022). [CrossRef]
18. Rivera-Arreba, I.; Bruinsma, N.; Bachynski, E.E.; Viré, A.; Paulsen, B.T.; Jacobsen, N.G. Modeling of a Semisubmersible Floating Offshore Wind Platform in Severe Waves. *J. Offshore Mech. Arct. Eng.* **2019**, *141*, 061905. [CrossRef]
19. Nematbakhsh, A.; Olinger, D.; Tryggvason, G. A Nonlinear Computational Model of Floating Wind Turbines. *J. Fluids Eng.* **2013**, *135*, 121103. [CrossRef]
20. Nematbakhsh, A.; Bachynski, E.E.; Gao, Z.; Moan, T. Comparison of wave load effects on a TLP wind turbine by using computational fluid dynamics and potential flow theory approaches. *Appl. Ocean. Res.* **2015**, *53*, 142–154. [CrossRef]
21. Li, H.; Bachynski, E. Experimental and numerical investigation of nonlinear diffraction wave loads on a semi-submersible wind turbine. *Renew. Energy* **2021**, *171*, 709–727. [CrossRef]
22. Li, H.; Bachynski, E. Analysis of difference-frequency wave loads and quadratic transfer functions on a restrained semi-submersible floating wind turbine. *Ocean Eng.* **2021**, *232*, 109165. . [CrossRef]
23. Galera-Calero, L.; Blanco, J.; Iglesias, G. Numerical Modelling of a Floating Wind Turbine Semi-Submersible Platform. *Appl. Sci.* **2021**, *11*, 11270. [CrossRef]
24. Xu, S.; Xue, Y.; Zhao, W.; Wan, D. A Review of High-Fidelity Computational Fluid Dynamics for Floating Offshore Wind Turbines. *J. Mar. Sci. Eng.* **2022**, *10*, 1357. [CrossRef]
25. Liu, Y. A CFD Study of Fluid Structure Interaction Problems for Floating Offshore Wind Turbines. Ph.D. Thesis, University of Strathclyde, Glasgow, UK, 2018.
26. Liu, Y.; Xiao, Q.; Incecik, A.; Peyrard, C.; Wan, D. Establishing a fully coupled CFD analysis tool for floating offshore wind turbines. *Renew. Energy* **2017**, *112*, 280–301. [CrossRef]
27. Zhou, Y.; Xiao, Q.; Liu, Y.; Incecik, A.; Peyrard, C.; Li, S.; Pan, G. Numerical Modelling of Dynamic Responses of a Floating Offshore Wind Turbine Subject to Focused Waves. *Energies* **2019**, *12*, 3482. [CrossRef]
28. Cheng, P.; Huang, Y.; Wan, D. A numerical model for fully coupled aero-hydrodynamic analysis of floating offshore wind turbine. *Ocean Eng.* **2019**, *173*, 183–196. [CrossRef]
29. Huang, Y.; Wan, D. Investigation of Interference Effects Between Wind Turbine and Spar-Type Floating Platform Under Combined Wind-Wave Excitation. *Sustainability* **2020**, *12*, 246. [CrossRef]

30. Tran, T.; Kim, D.H. A CFD study into the influence of unsteady aerodynamic interference on wind turbine surge motion. *Renew. Energy* **2016**, *90*, 204–228. [CrossRef]
31. Tran, T.; Kim, D.H. Fully coupled aero-hydrodynamic analysis of a semi-submersible FOWT using a dynamic fluid body interaction approach. *Renew. Energy* **2016**, *92*, 244–261. [CrossRef]
32. Tran, T.; Kim, D.H. A CFD study of coupled aerodynamic-hydrodynamic loads on a semisubmersible floating offshore wind turbine. *Wind Energy* **2018**, *21*, 70–85. [CrossRef]
33. Liu, Y.; Xiao, Q.; Incecik, A.; Peyrard, C. Aeroelastic analysis of a floating offshore wind turbine in platform-induced surge motion using a fully coupled CFD-MBD method. *Wind Energy* **2019**, *22*, 1–20. [CrossRef]
34. Arabgolarcheh, A.; Jannesarahmadi, S.; Benini, E. Modeling of near wake characteristics in floating offshore wind turbines using an actuator line method. *Renew. Energy* **2022**, *185*, 871–887. [CrossRef]
35. Zhang, Y.; Kim, B. A Fully Coupled Computational Fluid Dynamics Method for Analysis of Semi-Submersible Floating Offshore Wind Turbines Under Wind-Wave Excitation Conditions Based on OC5 Data. *Appl. Sci.* **2018**, *8*, 2314. :10.3390/app8112314 [CrossRef]
36. Gaertner, E.; Rinker, J.; Sethuraman, L.; Zahle, F.; Anderson, B.; Barter, G.; Abbas, N.; Meng, F.; Bortolotti, P.; Skrzypinski, W.; et al. *Definition of the IEA 15-Megawatt Offshore Reference Wind Turbine*; NREL/TP-5000-75698; National Renewable Energy Laboratory: Golden, CO, USA, 2020.
37. Allen, C.; Viselli, A.; Dagher, H.; Goupee, A.; Gaertner, E.; Abbas, N.; Hall, M.; Barter, G. *Definition of the UMaine VolturnUS-S Reference Platform Developed for the IEA Wind 15-Megawatt Offshore Reference Wind Turbine*; NREL/TP-5000-76773; National Renewable Energy Laboratory: Golden, CO, USA, 2020.
38. Kimball, R.; Robertson, A.; Fowler, M.; Mendoza, N.; Wright, A.; Goupee, A.; Lenfest, E.; Parker, A. Results from the FOCAL experiment campaign 1: Turbine control co-design. *J. Phys. Conf. Ser.* **2022**, *2265*, 022082. [CrossRef]
39. Mendoza, N.; Robertson, A.; Wright, A.; Jonkman, J.; Wang, L.; Bergua, R.; Ngo, T.; Das, T.; Odeh, M.; Mohsin, K.; et al. Verification and Validation of Model-Scale Turbine Performance and Control Strategies for the IEA Wind 15 MW Reference Wind Turbine. *Energies* **2022**, *15*, 7649. [CrossRef]
40. Siddiqui, M.; Hanssen, F.C.; Greco, M.; Anda, E. Investigation of CFD versus Potential-Flow Methods for Hydrodynamic Loads on a Floating Offshore Wind Turbine. In Proceedings of the 14th International Conference on Hydrodynamics, Wuxi, China, 21–25 October 2022.
41. de Vaal, J.B.; Muskulus, M. Simplified wake modelling for wind farm load prediction. *J. Phys. Conf. Ser.* **2021**, *2018*, 012012. [CrossRef]
42. Durakovic, A. World's Most Powerful Wind Turbine Starts Producing. Available online: https://www.offshorewind.biz/2021/12/10/worlds-most-powerful-wind-turbine-starts-producing/ (accessed on 15 January 2022).
43. DNV. *Sesam User Manual Wadam Wave Analysis by Diffraction and Morison Theory*; Technical Report; DNV: Hovik, Norway, 2017.
44. Shao, Y.L. Numerical Analysis of Second Order Mean Wave Forces by a Stabilized Higher-Order Boundary Element Method. *J. Offshore Mech. Arct. Eng.* **2019**, *141*, 051801. [CrossRef]
45. Jasak, H. Error Analysis and Estimation for the Finite Volume Method with Applications to Fluid Flows. Ph.D. Thesis, Imperial College: London, UK, 1996.
46. OpenFOAM. The Open Source CFD Toolbox v1906. 2019. Available online: https://www.openfoam.com/ (accessed on 30 March 2021).
47. Hirt, C.W.; Nichols, B.D. Volume of fluid (VOF) method for the dynamics of free boundaries. *J. Comput. Phys.* **1981**, *39*, 201–225. [CrossRef]
48. Higuera, P.; Lara, J.L.; Losada, I.J. Realistic wave generation and active wave absorption for Navier-Stokes models. Application to OpenFOAM®. *Coast. Eng.* **2013**, *71*, 102–118. [CrossRef]
49. Windt, C.; Davidson, J.; Schmitt, P.; Ringwood, J. On the Assessment of Numerical Wave Makers in CFD Simulations. *J. Mar. Sci. Eng* **2019**, *7*, 47. [CrossRef]
50. Jasak, H.; Tukovic, Z. Automatic mesh motion for the unstructured Finite Volume Method. *Trans. FAMENA* **2006**, *30*, 1–20.
51. Journée, J.; Massie, W. *Offshore Hydromechanics*, 1st ed.; Delft University of Technology: Delft, The Netherlands, 2001.
52. Faltinsen, O.M. *Sea Loads on Ships and Offshore Structures*; Cambridge University Press: Cambridge, UK, 1990.
53. Yang, L.; Nestegård, A.; Falkenberg, E. Analysis of Semi-submersible under Combined High Waves and Current Conditions Compared with Model Tests. In Proceedings of the ASME 2018 37th International Conference on Ocean, Offshore and Arctic Engineering, Madrid, Spain, 17–22 June 2018. [CrossRef]
54. DNV. *Recommended Practice, Environmental Conditions and Environmental Loads, DNV-RP-C205*; Technical Report; DNV: Hovik, Norway, 2010.

Disclaimer/Publisher's Note: The statements, opinions and data contained in all publications are solely those of the individual author(s) and contributor(s) and not of MDPI and/or the editor(s). MDPI and/or the editor(s) disclaim responsibility for any injury to people or property resulting from any ideas, methods, instructions or products referred to in the content.